Faculdade de Engenharia da Universidade do Porto

Atmospheric Wind Flow Distortion Effects of Meteorological Masts

Mohamed F. Lotfi

Master of Computational Mechanics

Supervisor: José M. L. M. Palma

October 27, 2015

Atmospheric Wind Flow Distortion Effects of Meteorological Masts

Mohamed F. Lotfi

Master of Computational Mechanics

October 27, 2015

Resumo

Distorção do campo de fluxo de vento causada por estruturas de rede complexas de mastros estaiadas pode resultar em significativa incerteza de medição do vento. Este problema é de importância prática na indústria de energia eólica, onde a qualidade da medição é de valor económico significativo, particularmente na avaliação de recursos eólicos. Neste estudo foram utilizados modelos numéricos e experimentais para simular o fluxo de distorção causado pela geometria da estrutura tridimensional de mastros meteorológicos. Simulações de CFD foram realizadas numa secção representativa de um mastro real usando software comercial Fluent. Simulações do campo de fluxo consideraram os efeitos de parâmetros de turbulência da corrente livre nas direções da camada limite atmosférica e vento. A validação dos resultados de CFD foi realizada por comparação com experimentos em túnel de vento de um modelo em escala reduzida da mesma secção usando o fio quente e filme de anemometria quente. Equação dupla RANS de modelação de turbulência foi utilizada para CFD e verificou-se que o modelo k-ω SST foi o mais adequado. Os resultados foram comparados com a norma do International Electrotechnical Comité (IEC) sobre o posicionamento da montagem dos anemómetros, bem como estudos publicados recentemente. O estudo propõe uma melhoria dos dados actualmente estabelecidos em relação à qualidade da medição com mastros meteorológicos e orientações para a colocação dos anemômetros.

Este trabalho foi realizado em colaboração com o Laboratório de Aerodinâmica e Calibração (LAC) em INEGI Porto.

Abstract

Distortion of the wind flow field caused by complex lattice structures of guyed masts can result in significant wind measurement uncertainty. This problem is of practical importance in the wind power industry where quality of measurement is of significant economic value, particularly in wind resource assessment. In this study numerical and experimental models were used to simulate the flow distortion caused by three-dimensional lattice geometry of meteorological masts. CFD simulations were performed on a representative section of a real mast using Fluent commercial software. Simulations of the flow field considered the effects of freestream turbulence parameters in the atmospheric boundary layer and wind directions. The validation of the CFD results was performed by comparison with wind tunnel experiments of a scaled-down model of the same section using hot wire and hot film anemometry. Two-equation RANS turbulence modeling was used for CFD and it was found that the k-ω SST model was the most suitable. The results were compared with the International Electrotechnical Committee (IEC) standard regarding the placement of anemometer mounting, as well as recently published studies. The study proposes an improvement of the currently established data regarding the quality of measurement with meteorological masts and guidelines for anemometer placement.

This work was performed in collaboration with the Laboratory of Aerodynamics and Calibration (LAC) in INEGI Porto.

Acknowledgments

First and foremost, I would like to sincerely thank my supervisor Prof. José Palma and the Master in Computational Mechanics program director Prof. José César Sá for their constant support and patience throughout my learning process. I would like to extend my gratitude to Eng. Miguel Marques the technical manager of LAC at INEGI Porto for his unlimited support and assistance during the course of this work. I would also like to express my gratitude to Dr. Carlos Rodrigues whose advice on many aspects were vital. My sincere thanks also go to all members of the wind energy group at INEGI Porto and in particular Luís Mendes for their technical assistance and support.

My family has always been extremely supportive and my extreme gratitude and appreciation for them go without saying. I would also like to thank my friend and colleague Helder Salvador, whose companionship during my studies was absolutely positive and joyful. Last but not least, I would like to thank my oldest and dearest friend Sana Ghouri, who never hesitated to support me during the toughest times of my studies.

Mohamed F. Lotfi

"Tudo vale a pena se a alma não é pequena."

Fernando Pessoa

Contents

List of Figures

List of Tables

Abbreviations and Symbols

Abbreviations

Abbreviation	Full Phrase
BL	Boundary Layer
CAD	Computer-Aided Design
CEN	European Committee for Standardisation
CFD	Computational Fluid Dynamics
CTA	Constant-Temperature Anemometer
DAQ	Data Acquisition
EN	European Standard
FEUP	Faculty of Engineering of the University of Porto
IEC	International Electrotechnical Commission
INEGI	Institute of Science and Innovation in Mechanical and Industrial Engineering
LAC	Laboratory of Aerodynamics and Calibration (INEGI)
RMS	Root Mean Square
TS	Test Section (Wind-Tunnel)
(U)RANS	(Unsteady) Reynolds-Averaged Navier-Stokes

Chapter 1

Introduction

1.1 Objective

Anemometers mounted on guyed structures are considered the standard setup for wind measurement. Two main types of those support structures exist: tabular towers and lattice masts. A major source of wind measurement uncertainty is due to complex wind flow distortion caused by lattice geometries of masts. The objective of this work is to use computational fluid dynamics and wind tunnel experiments to study those effects to quantify this uncertainty and suggest guidelines for mounting instruments. Adequate placement of instruments can minimize flow distortion effects and provide more accurate wind measurement.

1.2 Background and Motivation

Guyed lattice masts are employed in a wide variety of applications. Axial loading due to the weight of the mast is efficiently sustained by the lattice structure design. Transverse and torsional load components which are mainly induced by wind action are supported by guyed cables attached to the ground. This design greatly alleviates wind loading as a result of increased porosity when compared to the more traditional tabular (cylindrical) towers. As a result, greater heights can be achieved by guyed lattice masts. For these reasons, guyed lattice masts are commonly used as support structures for wind measurement instruments, allowing wind data to be obtained at high elevations from ground level. Three main reasons why wind measurements are needed at specific heights are:

Figure 1.1: Measurement instruments mounted on a guyed triangular lattice mast located near Viseu, Portugal.

- Ground obstacles such as bushes, trees, or buildings form what is known as the roughness height in atmospheric flows. When this layer is not in itself under study, measurements are often required beyond its height.
- Wind shear data is made available by taking simultaneous measurements at multiple heights along the mast, most useful in fluid dynamics and meteorology research.
- Measurements at the hub-height of wind turbines are a necessity in multiple applications ranging from resource assessment of potential sites, to performance monitoring of existing installations and control of turbine blades.

Power generated by a wind turbine is proportional to the cube of wind speed at turbine hub height (IEC, 2005). Accurate measurement of wind speed therefore has a significant impact on the wind energy industry since uncertainty in wind speed measurement would correspondingly

be cubed when associated with power calculation. An example of a decision greatly affected by this dependency is determining the economic viability of a potential wind farm site.

Cup and vane anemometers mounted on met masts* are the current standard setup for measuring wind speed and direction, respectively. Uncertainty of a measurement setup is a value expressing the maximum deviation a measured quantity is expected to be from the true one. Systematic and random errors decrease accuracy and precision of a measurement instrument, respectively, adding to uncertainty of acquired measurements. Systematic errors of anemometers are usually well accounted for by manufacturers and calibration laboratories. Therefore, anemometer uncertainty in met mast setups are mainly caused by random errors. Met masts themselves are employed as passive structures; their mere purpose is to maintain the position of instruments at desired heights and their presence should not affect the measurement process. If it does, the resulting error should be analyzed and eliminated if possible. Otherwise, the associated uncertainty should be quantified and taken into consideration when handling or analyzing the acquired data.

In recent years wind turbines have become increasingly larger in size and as a result typical hub heights are also increasing. This allows increased power output as greater wind speeds are encountered higher along the atmospheric boundary layer away from ground obstacles. In the past, tabular towers were sufficient to place measurement instruments at designated hub heights which were commonly up to 80 meters. However, lattice masts are constantly being employed to meet increasing hub-heights which now often exceed 100 meters. This advantage of met masts in making measurements at greater heights possible comes at a cost: interference of their complex lattice structure with the wind flow field. Indeed, tabular towers also have a flow distortion effect; however, it is possible to accurately determine and quantify the distortion due to their geometry. This is because interference effects of tabular towers can can be modeled as a modified case of the extensively studied problem of external flow around a cylinder. The much more complex interference with a lattice geometry however is not so easily quantifiable and has not been as widely studied in scientific literature. As a result, detailed and generally applicable information on the phenomenon are not widely available.

As mentioned, masts are employed as passive structures in the measurement process and therefore such distortion effects must be verified not to affect measurements acquired by mounted instruments. If they do, the nature and magnitude of this measurement error should be quantified, and all factors of which it is a function of identified. The resulting information including intensity of the distortion field, in addition to its dependency on structural and wind variables would be useful to improve the measurement process from two main perspectives:

*The shortened term *met mast* (meteorological mast) is used throughout this work to refer to guyed lattice masts solely employed as a support structure for meteorological measurement purposes.

- Measurement instruments can be placed outside the region where the wind is found to be most distorted, minimizing added uncertainty of acquired measurements. This is possible once the desired minimum level of accuracy is set.
- Given the instruments' location at the time of measurement in addition to factors affecting the interference (e.g., mast geometry and wind conditions), corrections can be applied to existing data, eliminating entirely or minimizing errors due to distortion effects.

Annex G of IEC standard 61400-12-1 (IEC, 2005) contains instructions for mounting cup anemometers outside the shadow zones[†] of support structures commonly employed in the field (tabular towers, triangular, and square masts). It provides the user an adequate distance from the mast at which anemometers should be placed in order to achieve a certain level of measurement accuracy. Although considered the prime reference for anemometer placement guidelines in the wind power industry, the standard does have its limitations in terms of information provided and their application scope. Recent publications, in particular (Fabre et al., 2014), have demonstrated using numerical simulations and wind tunnel experiments that improvements can be made and more details regarding distortion effects of the structures can be provided, using more modern techniques to obtain this information than those used by the standard.

Indeed, computational power and CFD codes have both been significantly upgraded since the last issue of (IEC, 2005). This led recent publications as well to recommend improvements in both the data provided by the standard and the methods used to obtain them, which have become outdated at the time of the current work. Recent literature has proven the potential of modern three-dimensional CFD software to model the real geometry of a lattice mast and simulate the resulting flow distortion with high accuracy. Such publications have been the main motivation behind the current work, which aims to identify and fill the gap about what factors are known to contribute to distortion effects of anemometer support structures.

1.3 Literature Review

At the time of the current work, available knowledge related to flow distortion effects of anemometer support structures could be classified in two categories: international standards such as (IEC, 2005) and recent scientific literature comprising mainly of conference proceedings and journal articles such as (Fabre et al., 2014). Since the structures used for anemometer placement are also employed in a broad spectrum of applications, many of those sources do not

[†]The term *shadow zone* refers to the volume in the vicinity of a structure where wind flow distortion effects are most significant. It is repeatedly used in scientific literature.

directly address the problem from a wind measurement perspective. However they do provide useful information regarding the more general problem of those structures subjected to wind action. Such sources were used as secondary references for this work, providing useful input for establishing the current state-of-the-art knowledge of the problem in addition to developing the numerical and experimental methodology proposed in this work.

In fact, few of the publications reviewed were found to address flow distortion effects; and even less were found to consider wind tunnel experiments or numerical modeling. Those studies are listed in Section 1.3.2 and the methods used summarized in Table 1.2. The objective was therefore to identify the limitations and aspects overlooked by previous work, aiming at filling the research gap.

1.3.1 International Standards

Three international standards were reviewed related to the current problem, including (IEC, 2005). The other two are Eurocode standards, addressing the same problem from a structural point of view. They provide definitions regarding the geometric properties of the structures in addition to expected loading caused by wind action. The standard numbers, titles, and relevant sections are listed below.

- **IEC 614200-12-1** Wind turbines – Part 12-1: Power performance measurements of electricity producing wind turbines (IEC, 2005).
  - Annex G is the only part of the standard which is directly relevant. It serves as an initial source of what is established in the wind power industry regarding met mast flow distortion effects and resulting effects on measurement quality of mounted instruments.
- **EN 1991-1-4** Eurocode 1 – Actions on structures - Part 1-4: General actions - Wind actions (CEN, 2005).
  - Section 5.3 of the standard provides a simple equation to calculate the wind force acting on an arbitrary structure. It can be applied to the case of lattice masts provided that the corresponding coefficients are used, which can be obtained from section 7.11 of the same standard in addition to B.2 of EN 1993-3-1.
  - Section 7.11 primarily provides the force coefficient for lattice structures as a function of solidity ratio and Reynolds number. It defines the calculation method for the last two.

- **EN 1993-3-1** Eurocode 3 – Design of steel structures - Part 3-1: Towers, masts and chimneys - Towers and masts. (CEN, 2006).
  - Annex B provides a long set of equations to calculate wind loading (static or spectral) for lattice structures and guyed masts.

Annex G of (IEC, 2005) provides guidelines for anemometer placement to achieve minimum measurement error due to flow distortion effects. Two possible anemometer mounting configurations are top and boom mounting. Top mounting involves placing the anemometer on top of the met mast by means of a long vertical tube and thus avoiding the shadow zone altogether; therefore it is the method recommended by the standard. However, top mounting is dependent on the total mast height which does not necessarily correspond to desired measurement heights. Also, it is often required to install instruments at multiple elevations along the mast. In such cases the alternative configuration, boom mounting, is used. It involves placing instruments along the sides of the mast by means of a mounting boom, a tube attached perpendicular to the mast. According to the standard, this method is associated with higher flow distortion compared to top mounting. This is because interference effects of both the mast structure and mounting booms need to be accounted for. Some information regarding interference effects of the mast geometry are given by the standard if boom mounting is to be used. In addition, some statements are made regarding factors affecting the distortion such as incident wind angle, and wind speed. Then, for both tabular tower and lattice mast geometries, a top-down view of a horizontal transept shows iso-speed lines of normalized wind speed to be expected in the vicinity of the tower or mast. In addition, an expression for velocity deficit upstream of the mast is given as a function of solidity ratio t (refer to Eq. 2.47). A user of the standard could therefore select a certain threshold for desired accuracy (e.g., maximum of 1% error due to flow distortion) and use the provided iso-speed plots and velocity deficit expressions as guidelines for adequate equipment placement.

Although this may seem a solution to the entire problem that has been put forward, Annex G of the standard does have its own shortcomings. Those are either factors that were not considered or problems associated with the methodology by which the information presented was obtained. Some, but not all, of those shortcomings have been addressed by recently published studies; and until they all have put under study the standard will remain a guideline to avoid the shadow zone as much as possible, rather than providing precise description of mast interference effects. Such a reference remains unavailable to this date. A list of all shortcomings of Annex G have been compiled and presented in the following list.

1. **Numerical Scheme Used:** To obtain the iso-speed plots of the wind flow field, two-dimensional Navier-Stokes numerical calculations were used. For tabular towers this

may be an adequate modeling scheme given their geometry's two-dimensional nature; however not so for a three-dimensional lattice geometry. To model the lattice geometry in a two-dimensional manner, actuator disk theory (also referred to as momentum theory) was used. The theory is credited to W. Rankine, A. Greenhill and R. Froude, and was developed in the late 19th century providing a mathematical model for propellers and rotors considered ideal actuator disks. The power required to drive the rotor or propeller was given in terms its geometric properties, thrust force, and air density. the IEC standard uses this theory to model the lattice mast, using an expression for thrust coefficient in terms of thrust force, reference air density, and reference area. The momentum deficit can be added to the numerical model as a pressure-velocity relationship (Kulunk, 2011). Two main problems are noted with this scheme. The first is uncertainty associated with two-dimensional approximation of a three-dimensional problem, not just in terms of the geometry but also of the flow field. The second, and more important, point is the use of a momentum sink approach rather than considering the actual geometry of the mast.

2. **Assumed Location:** The given velocity deficit expression is along an axis passing through the mast center and perpendicular to one of the mast faces. The reference orientation used correspond to incident wind also perpendicular to one of the mast's faces. As a result, the velocity deficit values are given along an upstream profile. This does not correspond to real installations where mounting booms are attached to the mast faces, perpendicular to reference wind direction.

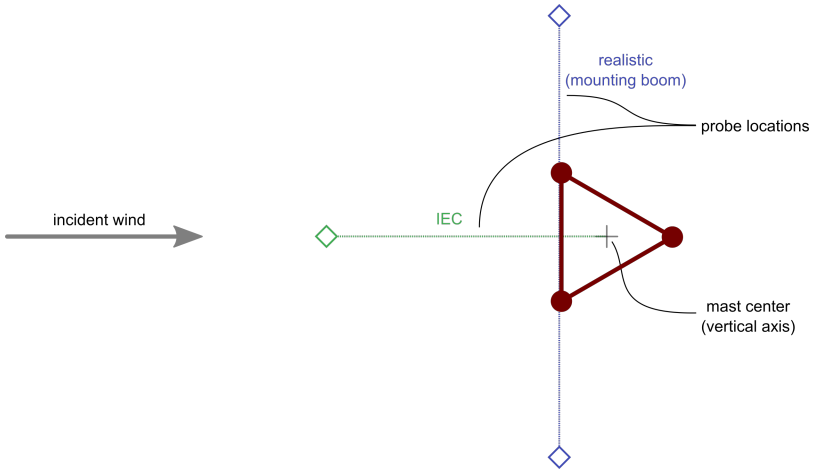

Figure 1.2: Illustration of boom locations: assumed by Annex G of (IEC, 2005) and realistic location.

3. **Global Applicability:** The velocity deficit expression is valid for a certain range of solidity ratio t which was explicitly specified by the standard. Many operational met masts have a solidity value outside the prescribed range, specifically when considering different incident

wind angles as the solidity ratio is a function therefore, as was demonstrated throughout this work. This brings into question how general the applicability of the given expression is.

4. **Angular Dependency:** Incident wind was considered perpendicular to one of the mast faces as in Fig. 1.2 and all information provided were confined to this orientation. The standard justifies this by stating that for a 90° measurement sector, this orientation is the one corresponding to least flow distortion. Three issues were noted here. First, no comparison criteria for the flow distortion was specified. If the velocity deficit expression was used for comparison, then the problem noted in the previous point of this list is encountered. Second, apart from mentioning that the aforementioned orientation results least flow distortion, no information was provided about effects of varying the orientation i.e., how much does flow distortion increase with varying wind directions and subsequent effect on boom length. Third, and most importantly, a 90° measurement sector does not span the entire 120° rotational symmetry angle of a triangular mast (refer to Section 2.2.2) which is a heavily employed type. I.e., according to geometric properties of a triangular lattice, a 90° is not sufficient to rule out other orientations which could result in less flow distortion.

5. **Velocity Dependency:** Dependency of the flow distortion on variation of wind speed was not discussed in detail by the standard. Indeed, all information is provided in dimensionless form however no mentioning of whether any velocity dependency exists for the flow field for a given range of Reynolds number. Since the flow distortion is foreseen as turbulent in nature, the self-similar nature of turbulence can imply that the same normalized velocity field would be obtained for the entire operating range of wind speed. This being a contemplation, it needs verification.

6. **Freestream Turbulence Dependency** Since even the tallest masts and towers still stand short of typical atmospheric boundary layer heights ($\delta = O(1km)$), wind speed and freestream turbulence surely vary along any given mast. Equipment mounted at different heights on the same mast would therefore be subject to different freestream conditions. Whether or not this would have an effect on the flow distortion was not considered by the standard and needs to be investigated.

With the IEC standard being nine years old at the time at which this work was commenced, limited computational resources available at the time would have meant that modeling the lattice geometry and conducting a comprehensive CFD study was not an efficient approach; and the methodology used would have been the an optimal one. Limited resources would have also limited the number of variables under study. Without the capacity to model the actual geometry and perform a three-dimensional analysis, considering the other mentioned (such as freestream turbulence) variables would not have been worthwhile. Since 2005 there have been

many advances in experimental and numerical fluid dynamics. Computational power and CFD codes have both been significantly upgraded which led recent publications to recommend improvements of the standard using various new approaches. In particular, the most recent publication on this matter (Fabre et al., 2014) has proven the potency of three-dimensional CFD simulations to model the actual geometry of a lattice mast simulate the resulting flow distortion. The obtained results were shown to provide guidance for placing instruments on the simulated mast comparable to the requirements given by Annex G of (IEC, 2005). In order to later compare obtained results with the standard, the given expressions and iso-speed contours are noted.

The expressions of thrust coefficient used by the IEC standard are summarized in Table 1.1. Given the geometry of a mast in question, the user can calculate the corresponding value for thrust coefficient and use Eq. 1.1 to obtain the (normalized) velocity profile upstream of the mast. The expression is given as a function of R/L, which is (normalized) leg distance. R corresponds to the distance upstream of the mast (in meters), and L is the mast leg distance (center-to-center distance between the legs). This normalized form of both distance and velocity deficit values provide a generalized guideline of expected distortion.

Table 1.1: Thrust coefficient expression used by (IEC, 2005) for different mast geometries.

Geometry	**Members**	**Thrust Coefficient**	**Validity Range**
Tabular	-	$C_T = 1.1$	$t = 1$
Triangular Lattice	Round	$C_T = 2.1(1-t)t$	$0.1 < t < 0.3$
Square Lattice	Round	$C_T = 2.6(1-t)t$	$0.1 < t < 0.3$
Square Lattice	Square	$C_T = 4.4(1-t)t$	$0.1 < t < 0.5$

$$U_d = 1 - \left(0.062C_T^2 + 0.072C_T\right) \cdot \left(\frac{L}{R} - 0.082\right) \tag{1.1}$$

By solving the previous equation for R, one can obtain an alternative form allowing the calculation of adequate anemometer separation given a desired measurement accuracy.

$$R = \frac{L}{\frac{1-U_d}{\left(0.062C_T^2 + 0.072C_T\right)} + 0.082} \tag{1.2}$$

This form is of more practical value in field application as the user can directly obtain the required boom length. It is often assumed that velocity deficit values on the sides of the mast would correspond to the same deficit upstream or at least that flow distortion encountered on the sides would be less than that present upstream. This would mean that the upstream values can be used, inherently considering some sort of safety factor.

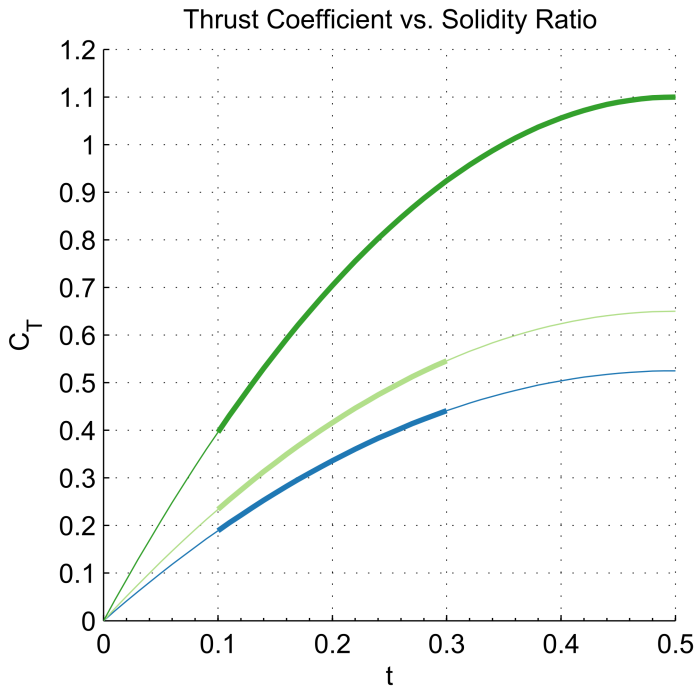

Figure 1.3: Thrust coefficient as a function of solidity of different mast geometries (triangular lattice in blue, square lattice with round members in light green, and square lattice with square members in dark green).

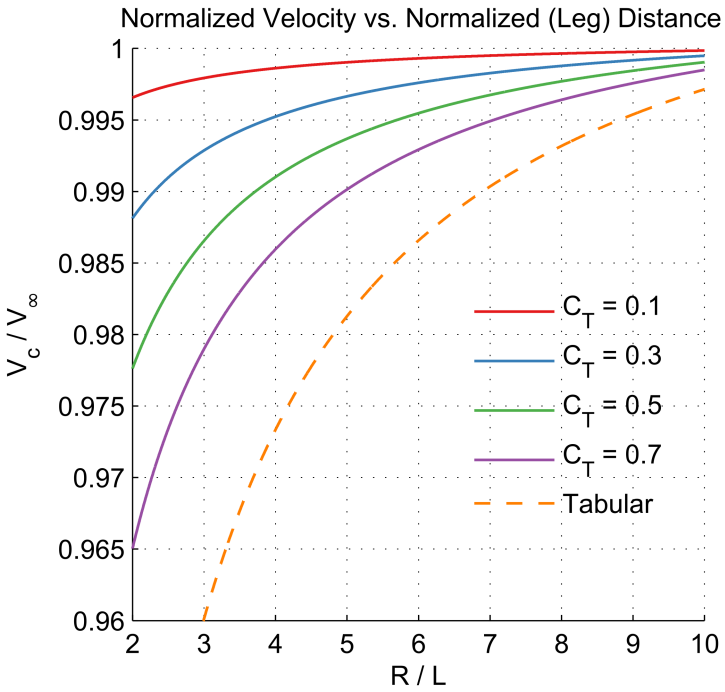

Figure 1.4: Velocity deficit values encountered upstream of a mast. Different upstream profiles are shown for varying thrust coefficient values, in addition to a tabular tower (corresponding to $C_T = 1.1$).

Fig. 1.3 and Fig. 1.4 show plots of the thrust coefficient and upstream velocity deficit, respectively. Since the thrust coefficient is a function of the square of solidity ratio, and velocity deficit is in turn a function of the square thereof, one could generally say that for increasing solidity ratio, a more intense distortion effect is to be encountered. The fact is (IEC, 2005) recommendations for anemometer mounting are therefore solely based on solidity of the structure in default configuration as per (CEN, 2005). This demonstrates the points described earlier, showing how factors such as angular dependency and freestream turbulence do not contribute to anemometer placement guidelines.

Fig. 1.4 also shows that tabular towers exhibit significantly higher velocity deficit values upstream than the worse case of lattice mast. It is important not to confuse the complexity of the flow distortion with its intensity. Compared to tabular towers, lattice masts cause a more complex distortion of the flow field due to their geometries in terms of its shape, size, and factors affecting it, however the intensity in terms of velocity deficit and speed-up values are lower compared with tabular towers.

The standard also contains iso-speed plots showing flow distortion values in the vicinity of the mast on a horizontal plane. Two plots are given showing a top-down view of the normalized velocity values: one for tabular towers and the other for lattice masts. No distinction was made for different lattice geometries or different solidity ratios, as one iso-speed plot was given for the case of a triangular lattice mast with corresponding to a thrust coefficient of 0.5. The iso-speed plots were digitized showing areas with flow distortion values greater than 1%. The digitized plots are shown in Fig. 1.5 and 1.6. By inspecting the plots, one can deduce that:

1. Tabular towers induce a significantly larger shadow zone both upstream and on the sides. Regions in the direct vicinity of the tower almost entirely exhibit flow distortion higher than 1%.

2. For lattice masts, a wider measurement sector could be utilized with minimum distortion effects. This would allow greater flexibility in anemometer installation.

3. The optimal boom location in the case of a tabular tower is at a 45° angle relative to incident wind. This is the only direction upstream of the mast which accurate measurement could be performed.

4. The optimal boom location in the case of a lattice mast would be perpendicular to incident wind direction and parallel to the mast face. This is in correspondence with what was previously demonstrated in Fig. 1.2.

5. Lattice masts exhibit a more intense flow distortion downstream. This can be attributed to the interacting wake effects of different members making up the lattice structure.

The previous observations in addition to the list of shortcomings presented earlier were set to be the focus of the current research work.

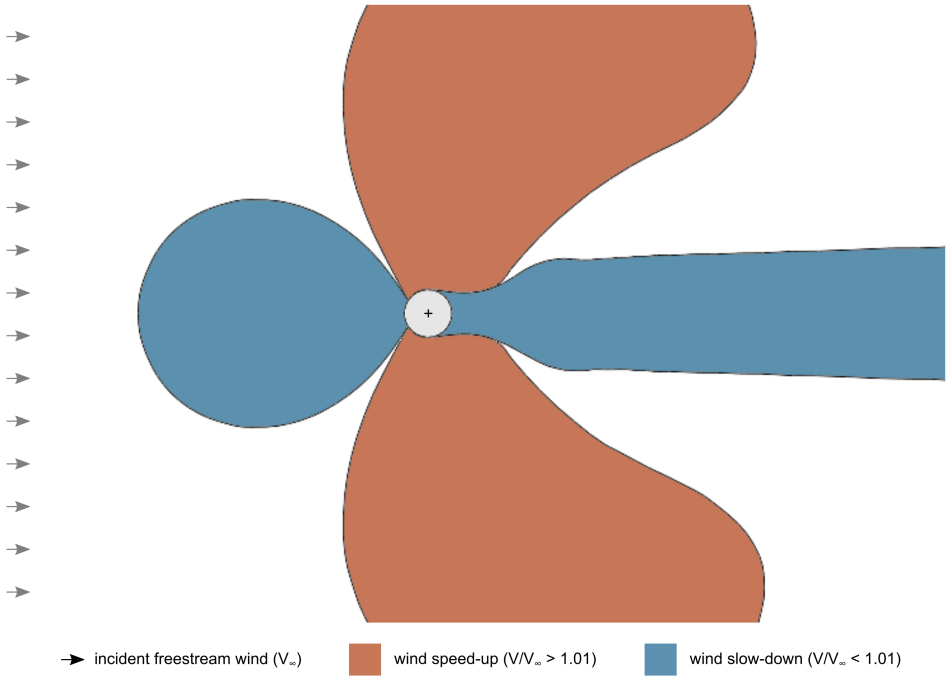

Figure 1.5: Digitized iso-speed plot for a tabular tower given by (IEC, 2005) . Areas with flow distortion error higher than ± 1% are shaded.

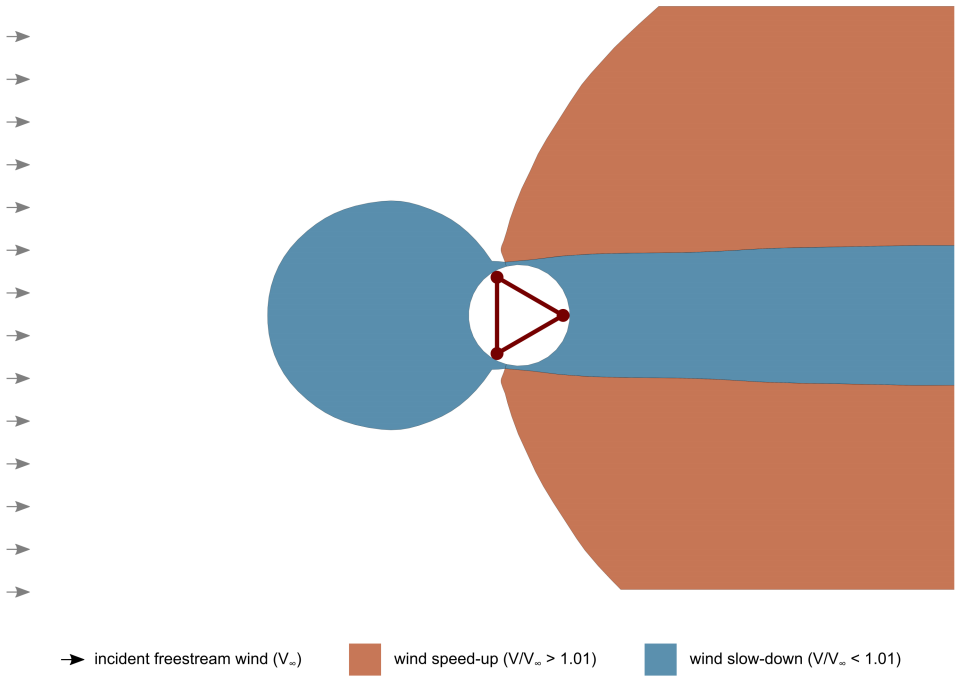

Figure 1.6: Digitized iso-speed plot for a lattice mast (triangular, $C_T = 0.5$ given by (IEC, 2005) . Areas with flow distortion error higher than ± 1% are shaded.

1.3.2 Recent Literature

This section presents a summary of reviewed studies related to the problem at hand. The scope of the conducted literature review was limited to studies made after the last publication of (IEC, 2005).

(Perrin et al., 2007) performed 3D CFD analysis to determine the measurement error of a top-mounted anemometer on a tabular tower using Fluent commercial software. Both cases of a hollow and solid tabular tower were considered. The hollow tower was modeled by using an expression for pressure gradient between the top and bottom of the tower. The effects of wind speed, turbulence intensity, and terrain slope were studied. Boom locations were considered for a full circle with steps of 30°. Their findings concluded that the difference in measurement error due to freestream turbulence intensity was not significant (<0.1%). The study concluded that to obtain a measurement error of less than 1%, a vertical separation of 5 tower diameters from the top should be maintained (for the more conservative case of a hollow tower).

(Lubitz, 2009) proposed a numerical model for flow distortion constructed by combining a (two-dimensional) Gaussian model of the turbulent wake and a potential flow solution outside the wake. The results were compared with field measurements taken from anemometers mounted on a lattice mast and a tabular tower. Effects of freestream turbulence or the actual geometry of a lattice mast were not considered as model inputs. The results have shown some agreement with field measurements, however it was suggested that the model simplicity posed significant limitations.

(Barlow et al., 2011) used wind tunnel experiments to study flow distortion effects of a lattice mast placed on top of the BT tower building in London, UK. The study used two different scaled-down models, to separately investigate the effects of the tower building and the lattice mast. Results were compared with field measurements taken on the course of two years. An upward deflection due to the tower building was observed, however was found to be minimal (<0.5%) at the height of mounted anemometers. The lattice tower itself was found to cause significant wind speed-up and flow distortion in terms of both measured speed and angle. Wind tunnel results were used to construct a correction of the field data. The study concluded that after applying the correction method, the field data could be reliably used.

(Tusch et al., 2011) was the oldest study found to consider atmospheric turbulence effects on flow distortion of both a tabular tower and a lattice mast. CFD analysis was performed using the $k-\omega$ SST two-equation RANS model. Atmospheric turbulence was considered by estimating the freestream turbulence intensity from standard deviation of wind speed field measurements (12.5% turbulence intensity was used). Turbulence length scale was based on Monin-Obhukov

profiles at a height of 50 meters. The actual geometry of the lattice mast was not modeled, rather using actuator-disk theory in the same manner as (IEC, 2005). The results showed greater wind speed deficit values than those given by (IEC, 2005), suggesting that the standard underestimated the distortion effects.

(Farrugia and Sant, 2013) studied the case of two cup anemometers mounted on opposite sides of a lattice mast located in Malta. The study used an existing method (Levenberg–Marquardt) to model measurements from one cup anemometer given the failure of the other. Field measurements over the course of one year were used to test the method used and modified by the study. Flow distortion effects on both anemometers caused by varying incident wind angles were investigated. The study concluded that the LM method was could be used to obtain missing data from a dysfunctional anemometer based on readings from the opposite one. The study also showed that eliminating wind speed measurements below 3 ms^{-1} could reduce the uncertainty of measurement.

(Pezo and Bakić, 2014) performed 3D CFD analysis of a lattice mast with the aim of determining the drag coefficient of the structure. Flow distortion effects were not considered by this study. The computational model consisted of one module of the mast. RANS turbulence models were used and the results were compared with experimental results and values given by (CEN, 2005) and showed good agreement with both. The study concluded that CFD analysis with RANS turbulence models could be used to accurately determine drag coefficient of a lattice structure.

(Fabre et al., 2014) was the only study found to use 3D CFD simulations to study flow distortion effects of a lattice mast by modeling its actual geometry. The FINO3 triangular lattice met mast was used as the test case. The study performed a sensitivity study of two-equation RANS models and found that the $k-\omega$ SST model performed best by comparison with wind tunnel experiments performed on a scaled-down model of the same mast. Turbulence effects were included by estimating turbulence intensity (5%) and setting the length scale as a factor of computational domain size. Flow distortion effects upstream of the mast were fount slightly higher than those given by (IEC, 2005) (the standard slightly underestimated distortion effects). However, considering different wind incident angles the study showed that shorter boom lengths than those recommended by (IEC, 2005) could correspond to the same measurement error.

The studies used as direct references for this work were ones which studied the distortion effects of lattice masts in particular. Table 1.2 summarizes the methods of analysis used by those studies.

It can be seen that only very recently, namely in the case of (Fabre et al., 2014), have 3D CFD simulations modeling the actual geometry been utilized. As such, the work of (Fabre et al., 2014) and (IEC, 2005) were considered the primary references for this work. The methodology used

Table 1.2: Recently published work on flow distortion caused by lattice met masts.

Previous Work	CFD (Full Geometry)	Actuator Disk Theory	Wind Tunnel Experiment	Field Measurement
(IEC, 2005)	-	✓	-	-
(Lubitz, 2009)	-	-	-	✓
(Barlow et al., 2011)	-	-	✓	✓
(Tusch et al., 2011)	-	✓	-	✓
(Farrugia and Sant, 2013)	-	-	-	✓
(Fabre et al., 2014)	✓	-	✓	-

by (Fabre et al., 2014) was used as an initial guide to developing the methods used in the current work, and is cited throughout this text. Final discussion of the results of this work includes a comparison with the previous studies cited above.

1.4 Problem Statement

Having identified the focus of this work as the study of flow distortion caused by met masts and subsequently providing improvements for anemometer placement guidelines in IEC standard; the problem needs to be formally defined in a scientific manner. To achieve the anticipated goals, a thorough study of interference of mast geometries with the wind flow field should be performed. A combination of wind tunnel experiments on a scaled-down model and numerical computations using commercial CFD software ANSYS Fluent can be used to replicate the real problem.

The first step of any research work is to put together a statement of hypothesis, defined as "an idea or explanation of something that is based on a few known facts but that has not yet been proved to be true or correct". Scientific research further requires that evidence obtained to support the hypothesis must be both 1) observable and 2) performed in a manner repeatable by others. The hypothesis made for the current work was:

> "Computational fluid dynamics simulations and wind tunnel experiments can be used to determine guidelines for cup anemometer placement on met masts that ensure minimum measurement error caused by wind flow distortion in the shadow zone".

The shortcomings listed in the previous section which highlighted key aspects in question in the IEC standard were defined as the primary factors to be focused on while constructing the methods of investigation. To further define the scope of the investigation, the following assumptions were made:

- Guyed cables were assumed to have negligible effects on the shadow zone. This assumption is valid given that instruments are not placed in the wake of any of the cables as per the IEC standard recommendation.
- Effects of structural deformation were assumed negligible i.e. the met mast was considered a rigid structure allowing a purely fluid dynamics study to be the case.
- A study of the shadow zone's transient and unsteady behavior would not offer any contribution to the current purposes. An average solution of the flow field is needed. Since turbulent flow is anticipated this has a direct effect on the choice of numerical models used.
- The interference effects of mounting booms were considered to have no effect on the shadow zone (i.e., the interference effects of the met mast and the mounting booms were assumed to be uncoupled and independent).

The effects limited by the last three would be best investigated in separate studies following up on this work as they require either a complex computational analysis (e.g., aeroelastic analysis to study structural deformation effects); or a thorough parametric investigation (e.g., many combinations of different mast and boom geometries need to be considered in order to make useful, non-case-specific conclusions).

A real triangular met mast located in Aboadela, Portugal was chosen as the study case. The proposed methodology was to first design a scaled-down model on which wind tunnel experiments could be performed. Afterwards, a CFD model would be constructed and refined, evaluating its accuracy by means of validation and verification tests. The following list of tasks to be performed was defined:

1. Conduct a **literature review**, surveying publications related to the current problem.
2. Model current met-mast using **CAD** software and **simplify geometry** for CFD use.
3. **1st CFD** experiment set: **designing scaled-down model**.
4. Prepare wind-tunnel experiment: **manufacture scaled-down mast** and **setup measurement equipment**.
5. Conduct **wind-tunnel experiment set**.
6. **2nd CFD** experiment set: **simulation of wind-tunnel experiment**.
7. **3rd CFD** experiment set: **simulation of full-scale case**.

8. **Validate** CFD model by means of numerical tests (ex. grid-dependency test) and by comparison of scaled-down and full-scale CFD and wind-tunnel experiment results.
9. **4^{th} CFD** experiment set: run parametric **studies on variables of interest** using validated CFD model.
10. **Analize** results, draw **conclusions**, and **report** findings.

1.5 Thesis Structure

This thesis was written in an IMRaD (Introduction, Methods, Results, and Discussion) report format corresponding to chapters 1, 2, 3, and 4, respectively.

Chapter 2 explains the tools used to investigate the problem and is divided in four sections. Section 2.1 defines the theoretical background relevant within the scope of this work. Section 2.2 presents the mast chosen as the test case for analysis and its geometrical details. Section 2.3 shows the set-up of wind tunnel experiments and measurement locations. Finally, Section 2.4 demonstrates the details of the CFD model used and grid independence studies.

Chapter 3 contains the results obtained, including preliminary ones. The first section (Section 3.1) demonstrates the design of the scaled-down model for wind-tunnel experiments. Despite being part of developing the methodology, it has been included in this chapter as the design process included preliminary CFD results. Section 3.2 contains a study of freestream conditions and their effect on the current problem, highlighting the importance of setting proper turbulence conditions in CFD analysis. Section 3.3 shows the validation of CFD results and choice of appropriate turbulence model by comparison with wind tunnel measurements. Next, the variation of flow conditions corresponding to the atmospheric boundary layer along the height of the mast is studied and shown in Section 3.4. Finally, the dependence on incident wind angle is investigated in Section 3.5 for both triangular and square lattice geometries.

Chapter 4 is the final chapter and presents a discussion of the results. Conclusions are made and limitations of the current work are duly pointed out. Finally, recommendations for future studies following up on this work are suggested.

Chapter 2

Methods

A considerable amount of focus was allocated for establishing a proper methodology to investigate the current problem, constantly verifying and validating different theories employed throughout the work. For wind tunnel experiments the biggest challenge was in designing the scaled-down model which would be suitable to replicate desired phenomena. For CFD simulations the challenge was in constructing a suitable and consistent numerical model. A flowchart of all the tasks performed and their dependencies is shown in Fig. 2.1. The flowchart shows two highlighted blocks, classifying the tasks performed to obtain final results in two categories: numerical (CFD analysis) and experimental (wind tunnel). As seen in the figure, an iterative process was performed to refine the numerical model used. This is not reported in full detail as many modifications are not relevant to the outcome of the work. However, major choices made in constructing the final numerical model were stated along with corresponding justifications. Those are comprised of the main elements of a CFD model: representative geometry, design of the grid structure, boundary conditions, turbulence model, etc.

This chapter begins in Section 2.1 by defining the theoretical fluid dynamics background related to the current problem, focusing on turbulence modeling, atmospheric boundary layers, and experimental aerodynamics. The mast chosen as the study case is then analyzed in Section 2.2 and all relevant geometric properties are calculated or identified. Next, the procedure followed to conduct the wind tunnel experiments is explained in Section 2.3 along with information about equipment used such as wind tunnel properties, sensors used, etc. Finally, the last section, Section 2.4, of this chapter explains the final CFD model used to obtain the results from which the conclusions are drawn. The final results were not shown in this chapter but rather all compiled and shown in Chapter 3.

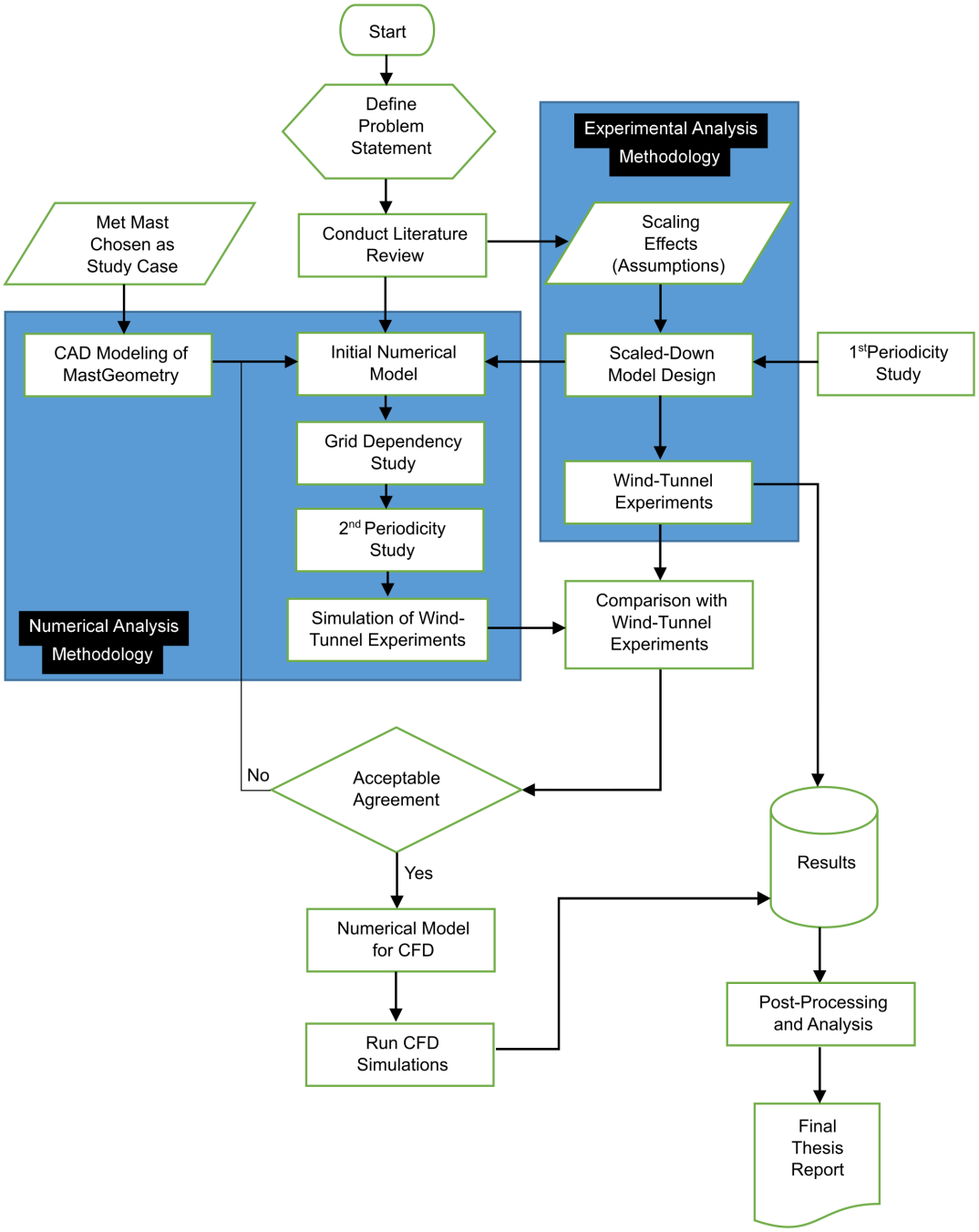

Figure 2.1: Work flowchart showing blocks corresponding to preparatory tasks, experimental analysis, CFD modeling, and reporting stages along with their dependencies.

2.1 Theoretical Background

2.1.1 Generalized Transport Equation

Fluid dynamics and thermal heat transfer problems are governed by conservation laws.

$$\text{div}\,\mathbf{I} = \left(I_x + \frac{\partial I_x}{\partial x}dx\right) - I_x + \left(I_y + \frac{\partial I_y}{\partial y}y\right) - I_y + \left(I_z + \frac{\partial I_z}{\partial z}dz\right) - I_z \tag{2.1}$$

$$\text{div}\,\mathbf{I} = \frac{\partial I_x}{\partial x} + \frac{\partial I_y}{\partial y} + \frac{\partial I_z}{\partial z} \tag{2.2}$$

Four independent variables exist: three spatial coordinates and time. The choice of a reference coordinate system can vary as long as certain rules are followed. However, Cartesian coordinates are used for the current work. For an arbitrary dependent variable $\phi(x, y, z, t)$, the general form of differential equations for conservation laws can be found to be as follows (Patankar, 1980).

$$\frac{\partial}{\partial t}(\rho\phi) + \text{div}\,(\rho\mathbf{V}\phi) = \text{div}\left(\Gamma_\phi\ \text{grad}\ \phi\right) + S_\phi \tag{2.3}$$

The differential equation which constitutes the generalized balance principle for a system under a conservation law contains four separate terms. Each term corresponds to a certain factor influencing the dependent variable.

- **Unsteady Term** - $\frac{\partial}{\partial t}(\rho\phi)$:
  The unsteady term accounts for the change of the dependent variable due to time evolution. ρ is the fluid density.

- **Convection Term** - $\text{div}\,(\rho\mathbf{V}\phi)$:
  The convection term accounts for the transport of the dependent variable due to the flow currents as the net efflux of the variable multiplied by the velocity field, $\mathbf{V} = [V_x, V_y, V_z]$.

- **Diffusion Term** - $\text{div}\left(\Gamma_\phi\ \text{grad}\ \phi\right)$:
  This term accounts for transport of the dependent variable due to diffusion. The equation assumes that diffusion is driven by the gradient of the dependent variable, which is suitable for most problems. Γ_ϕ is the diffusion coefficient and can be used to adjust the diffusion term depending on the specific process under study.

- **Source Term** - S_ϕ:
  This term could be used to model any internal effects which cannot be adequately expressed by the previous term. It could also account for any "external" sources (or sinks) of the variable quantity e.g., momentum added by a fan, or heat added by filament, etc.

This generalized differential equation is often referred to as the transport equation. Three conservation laws provide the governing equations for any fluid dynamics problem. The three quantities conserved are mass, momentum, and energy.

2.1.2 Mass Continuity

The continuity equation describes the principle of mass conservation in a fluid dynamics problem.

$$\frac{\partial \rho}{\partial t} + \operatorname{div}(\rho \mathbf{V}) = 0 \tag{2.4}$$

By comparison with the generalized transport equation one can see that for a general case, mass conservation is influenced by unsteady effects and convection transport. Applying the definition of divergence in Eq. 2.2 yields an alternative form of the continuity equation in Einstein notation by summation over $i = \{1, 2, 3\}$.

$$\frac{\partial \rho}{\partial t} + \frac{\partial (\rho V_i)}{\partial x_i} = 0 \tag{2.5}$$

For low Mach number ($M < 0.2$) flows, fluid compressibility effects can be assumed sufficiently small and can thus be neglected implying constant fluid density. As a result, the first term (temporal rate of change of density) is dropped, and the equation is simplified as follows.

$$\operatorname{div}(\rho \mathbf{V}) = \nabla \cdot \mathbf{V} = 0 \tag{2.6}$$

2.1.3 Navier-Stokes Equations

The Navier-Stokes equations are considered the fluid dynamics counterpart of Newton's second law for solid mechanics. The Navier-Stokes equations represent conservation of momentum in

a flow field. However, they remain one of the most complex mathematical equations used in physics. This is due to the fact that although given a complete set of initial and boundary conditions along with fluid properties a solution can be obtained, however a mathematical proof that a closed-form analytical solution exists is yet to be found. In other words, not only does a general solution of the Navier-Stokes equations not exist, neither does a proof of one existing therefore. This complexity arises from the same mathematical terms which give rise to the problem of turbulence. Indeed, the mathematical complexity of the equations is directly related to the turbulence phenomenon, and is the reason why the phrases "Navier-Stokes Problem" and "Turbulence Problem" are often interchanged when referring to the issue of mathematical complexity of the equations and the lack of a mathematical proof for a closed-form solution.

With momentum being the dependent variable, the equations are constructed for velocity (which is specific momentum, momentum per unit of mass). The Navier-Stokes equations are therefore a set of three equations, and is presented below for a non-compressible flow field.

$$\frac{\partial \mathbf{V}}{\partial t} + \mathbf{V} \cdot \nabla \mathbf{V} = \nu \nabla^2 \mathbf{V} - \frac{\nabla \mathbf{P}}{\rho} \tag{2.7}$$

One realizes the four terms are present: unsteady, convection, diffusion, and a source term. In this case, the source term represents an internal effect: forces due to the pressure field. If one multiplies by the density, the left-hand side of the equation would represent the inertia per unit volume of the fluid. The right-hand side would represent the forces acting on the fluid, and thus the correspondence with Newton's second law of motion.

The second (convection) term $\mathbf{V} \cdot \nabla \mathbf{V}$, is the reason for the mathematical complexity of the Navier-Stokes equations and is the main mathematical reason for the existence of the turbulence problem. Even though, the derivation from Newton's second law can still be observed: the left-hand side of the equation represents the fluid acceleration, while the right-hand side contains the forces per unit mass.

2.1.4 Viscosity Effects

The two phenomena related to viscosity which are within the scope of the current work are boundary layer theory and turbulence. It is important to note that the two are not mutually exclusive: a boundary layer can itself be laminar or turbulent. Both concepts are greatly intertwined especially within the scope of the current work, where met masts are present within the atmospheric boundary layer and themselves generate turbulent flow regimes.

Boundary layer theory is the essence and backbone of atmospheric wind profile theories for CFD modeling. The entire problem under study is one which exists within a boundary layer: the atmospheric one; and since investigating freestream turbulence effects is one of the current objectives, one must obtain an understanding of both phenomena and their effect on each other.

The significance of viscosity effects in a flow field can be quantified using Reynolds number.

$$Re = \frac{\text{Inertial Term}}{\text{Viscous Term}} \tag{2.8}$$

Note that as mentioned previously, the inertial and viscous terms correspond to the left and right hand sides of Eq. 2.7, respectively. Low Reynolds number flows occur when inertial forces are overpowered by viscous ones. This is the case of laminar flow fields characterized by "streamlined" velocity fields. On the other hand, a high Reynolds number flow results when inertial effects dominate viscous ones. In such cases turbulent flows are encountered, characterized by eddies and sinuous flows.

2.1.5 Turbulent Flows

Turbulent flows remain one of the most complex problems of physics due to the mathematical complexity of the governing equations. Reynolds decomposition is a technique developed in the late 19th century and is widely used in engineering models of turbulence. It argues that any flow field is inherently made up of two regimes: one laminar and one turbulent. The laminar effects are represented by a steady or (time-averaged) component, while the turbulent ones are represented using an unsteady or fluctuating component. Superposition of both terms yields the complete flow regime.

$$\mathbf{V}(x,y,z,t) = \overline{\mathbf{V}}(x,y,z) + \mathbf{V}'(x,y,z,t) \tag{2.9}$$

$$\mathbf{P}(x,y,z,t) = \overline{\mathbf{P}}(x,y,z) + \mathbf{P}'(x,y,z,t) \tag{2.10}$$

This is the first step to constructing what is known as the Reynolds-Averaged Navier-Stokes (RANS) model. Substituting the decomposed expressions in the Navier-Stokes equations gives rise to an extra term which is the Reynolds stress tensor. This accounts for momentum transport due to the fluctuating component i.e., momentum transport due to flow turbulence.

Solving this Reynolds stress term poses the main challenge when solving RANS equations. (Bachalo and Johnson, 1986) managed to solve the term by considering its time variation. The obtained expression is a function of the third moment $\overline{V_i' V_j' V_k'}$, which in itself can be solved for as function of the fourth moment, etc. For engineering applications, one needs to obtain an efficient formulation to "close" this set of infinite equations. This is referred to as the closure equation(s), and is the main distinguishing factor between different RANS models. The most prevailing turbulence model, $k-\epsilon$, models turbulence kinetic energy and dissipation rate (k and ϵ, respectively) as transported variables in the flow field. Two transport equations are used (ANSYSInc., 2011).

$$\frac{\partial}{\partial t}(\rho k) + \frac{\partial}{\partial x_i}(\rho k V_i) = \frac{\partial}{\partial x_j}\left[\left(\mu + \frac{\mu_t}{\sigma_\kappa}\right)\frac{\partial k}{\partial x_j}\right] + G_k + G_b - \rho\epsilon - Y_M + S_k \tag{2.11}$$

$$\frac{\partial}{\partial t}(\rho \epsilon) + \frac{\partial}{\partial x_i}(\rho \epsilon V_i) = \frac{\partial}{\partial x_j}\left[\left(\mu + \frac{\mu_t}{\sigma_k}\right)\frac{\partial \epsilon}{\partial x_j}\right] + C_{\epsilon 1}\frac{\epsilon}{k}\left(G_k + C_{\epsilon 3 G_b}\right) - C_{\epsilon 2}\rho\frac{\epsilon^2}{k} + S_\epsilon \tag{2.12}$$

Six constants are used by the $k-\epsilon$ model. Those constants are variables which are often set as the default values for the model (Pope, 2000; ANSYSInc., 2011).

$$\left\{C_\mu, C_{\epsilon 1}, C_{\epsilon 2}, C_{\epsilon 3}, \sigma_\kappa, \sigma_\epsilon\right\} = \{0.09, 1.9, 1.45, 0.8, 1.0, 1.3\} \tag{2.13}$$

The turbulence kinetic energy can be expressed as a function of flow velocity and turbulence intensity. The latter is a parameter often used when dealing with RANS modeling of turbulent flows and is defined as the ratio of the fluctuating components to the mean component of velocity.

$$k = \frac{3}{2}(\overline{V} I)^2 \tag{2.14}$$

$$I = \frac{V'}{\overline{V}} \tag{2.15}$$

The turbulence dissipation rate, ϵ, is defined as the rate at which kinetic energy of turbulence is converted to thermal energy due to viscous effects. It can be expressed as a function of k and length scale l.

$$\epsilon = \frac{C_\mu^{-0.25} k^{1.5}}{l} \tag{2.16}$$

Same way turbulence intensity (or kinetic energy) describes the temporal properties of the fluctuating components causing turbulence, the length scale describes the spatial variation in turbulence i.e., spatial size of turbulent eddy structures. Thus turbulence is modeled with its unsteady nature in both temporal and spatial scales, coupled by the above expression for ϵ.

Another commonly employed two-equation turbulence model is the Wilcox $k-\omega$ model using specific turbulent dissipation rate, ω, instead of ϵ to account for spatial properties of turbulence and is defined as the reciprocal of ϵ.

$$\omega = \frac{1}{\epsilon} \tag{2.17}$$

A disadvantage of the $k-\omega$ model is the fact that computational grids need to be refined near the walls (down to the viscous sublayer with dimensionless wall distance $y^+ \sim 1$). Although this is quite useful when near-wall flow fields are of interest it greatly adds to the computational cost of the CFD analysis. A variation of the $k-\omega$ model is the $k-\omega$ SST (shear stress transport) model which provides an efficient work-around this problem, using a blending function which activates the $k-\omega$ model near the wall, and uses the standard $k-\epsilon$ model further towards the freestream. This combines the advantages of both models, and is for that reason why the $k-\omega$ SST model has been proven to perform particularly well with external flow problems (ANSYSInc., 2011). The following equations are used.

$$\frac{\partial}{\partial t}(\rho k) + \frac{\partial}{\partial x_i} + (\rho V_i k) = \tilde{P}_k - \beta \rho k \omega + \frac{\partial}{\partial x_j}\left[(\mu + \rho_k \mu_t)\frac{\partial k}{\partial x_i}\right] \tag{2.18}$$

$$\frac{\partial}{\partial t}(\rho\omega) + \frac{\partial}{\partial x_i}(\rho V_i \omega) = \alpha \rho S^2 - \beta \rho \omega^2 + \frac{\partial}{\partial x_j}\left[(\mu + \sigma_\omega \mu_t)\frac{\partial \omega}{\partial x_i}\right] + 2(1-F_1)\rho\sigma_{\omega 2}\frac{1}{\omega}\frac{\partial k}{\partial x_i}\frac{\partial \omega}{\partial x_i} \tag{2.19}$$

The blending function F_1 is defined as follows (Fabre et al., 2014; ANSYSInc., 2011).

$$F_1 = \tanh\left\{\left\{\min\left[\max\left(\frac{\sqrt{k}}{\beta^*\omega y}, \frac{500\nu}{y^2\omega}\right), \frac{4\rho\sigma_{\omega 2}k}{CD_{k\omega}y^2}\right]\right\}^4\right\} \tag{2.20}$$

2.1.6 Atmospheric Boundary Layer

Boundary layers form when a viscous fluid moves past a solid surface or wall. Friction is induced between the surface and the layer of fluid directly in contact with the wall. This "skin friction" causes a shear stress to act on the fluid and thereby creating a shear stress gradient. The friction causes the fluid velocity to significantly drop at the wall (a non-slip condition). Depending on the surface roughness the value of the velocity at the wall (also referred to as friction velocity) varies. Roughness effects are modeled by a roughness height, normal to the wall surface. Within this layer the flow field is not considered, and the velocity is assumed to be equal to V_w, increasing gradually as a function of shear stress as one moves towards the freestream.

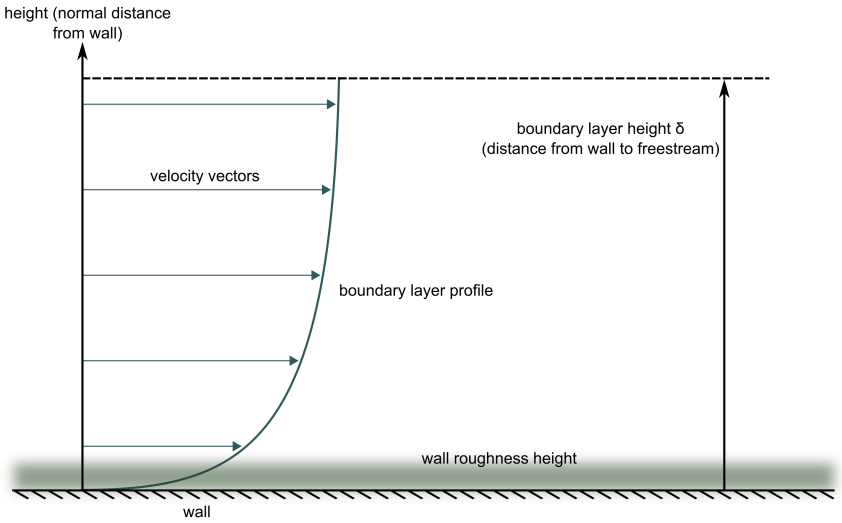

Figure 2.2: Boundary layer profile near a wall with a constant roughness height.

Atmospheric flows are a real-life example of a boundary layer flow. Wind flowing close to the earth's surface is affected by roughness caused by terrain ruggedness, obstacles such as trees or forests, or man-made obstacles such as buildings. Existing theories which provide simplified expressions for boundary layer profiles to be used as inlet conditions for CFD modeling of atmospheric flows. Some of the commonly used ABL profile theories for CFD are listed, with the corresponding expressions for $V_z(y)$, $k(y)$, and $\epsilon(y)$ shown.

- (Richards and Hoxey, 1993)

$$V_z(y) = \frac{V^*}{\kappa} ln\left(\frac{y}{y_0}\right) \tag{2.21}$$

$$k(y) = \frac{V^{*2}}{\sqrt{C_\mu}} \tag{2.22}$$

$$\epsilon(y) = \frac{V^{*3}}{\kappa y} \tag{2.23}$$

The von Kármán constant, κ can be determined as a function of the $k-\epsilon$ model constants.

$$\kappa = \sqrt{(C_{\epsilon 2} - C_{\epsilon 1})\,\sigma_\epsilon \sqrt{C_\mu}} \tag{2.24}$$

Although the same profiles can be used regardless of specific two-equation turbulence model chosen, the following expression can be used for ω instead of ϵ in case the $k-\omega$ model is chosen:

$$\omega(y) = \frac{V^*}{\sqrt{\beta'}\kappa y} \tag{2.25}$$

In this case, κ is evaluated as a function of the $k-\omega$ model constants.

$$\kappa = \sqrt{\frac{(\beta - \alpha\beta')}{\sqrt{\beta'}}} \tag{2.26}$$

- (Eidsvik, 2008)

$$V_z(y) = \frac{V^*}{\kappa} ln\left(\frac{y}{y_0}\right) \tag{2.27}$$

$$k(y) = \frac{V^{*2}}{\sqrt{C_\mu}}\left(1 - \frac{y}{\delta}\right)^2 \tag{2.28}$$

$$\epsilon(y) = \frac{V^{*3}}{\kappa y}\left(1 - \frac{y}{\delta}\right)^2 \tag{2.29}$$

Where l_m is calculated in accordance with (Blackadar, 1962):

$$\frac{1}{l_m} = \frac{1}{\kappa y} + \frac{1}{\kappa(\delta - y)} = \frac{1}{l^*} + \frac{1}{l_\delta} \tag{2.30}$$

- (Palma et al., 2008)

$$V_z(y) = \frac{V^*}{\kappa} ln\left(\frac{y}{y_0}\right) \tag{2.31}$$

$$k(y) = \frac{V^{*2}}{\sqrt{C_\mu}}\left(\frac{l_m}{\mathcal{L}}\right)^2 \tag{2.32}$$

$$\epsilon(y) = \frac{V^{*3}}{\mathcal{L}}\left(\frac{l_m}{\mathcal{L}}\right)^3 \tag{2.33}$$

$$l_m = min\left\{\kappa y, C_\mu \delta\right\} \tag{2.34}$$

$$\mathcal{L} = \begin{cases} \kappa y & y < \delta \\ \delta & y \geq \delta \end{cases} \tag{2.35}$$

The above mentioned profile theories can be used to determine freestream turbulence conditions which an operating met mast would be exposed to.

2.1.7 Experimental Aerodynamics

Wind tunnels are used in experimental aerodynamics to study external flow around solid objects. Wind tunnels can be classified according to multiple factors such as size, working speed, and assembly. The last refers to the sequence of components of a wind tunnel and results in two main types of tunnels: open and closed circuit. In open circuit wind tunnels, wind is enters the tunnel, passes through its various chambers, and is exhausted at the end. In closed circuit wind tunnels, the air is recirculated back rather than exhausted, hence the name. The wind tunnel used for this study was an open circuit wind tunnel and thus is the type which will be discussed.

In general, the main components of an open circuit wind tunnel are (in order, upstream to downstream):

1. inlet (fan) section,
2. settling chamber,
3. contraction region,
4. test section, and
5. diffuser section.

The contraction ratio is defined as the ratio of inlet to outlet areas of the contraction region. All velocity variations caused by the contraction region can be calculated using this ratio (Mehta and Bradshaw, 1979; Bell and Mehta, 1989).

$$c = \frac{A_1}{A_2} \tag{2.36}$$

- mean velocity in z- direction (freestream component)

$$\frac{1}{c} = \frac{\bar{V}_{1,z}}{\bar{V}_{2,z}} \tag{2.37}$$

- mean velocity in x- and y- directions (cross-flow components)

$$\sqrt{c} = \frac{\bar{V}_{1,x}}{\bar{V}_{2,x}} = \frac{\bar{V}_{1,y}}{\bar{V}_{2,y}} \tag{2.38}$$

- RMS intensity of z-velocity

$$\frac{1}{2c} \cdot 3\left(ln\left(4c^3\right) - 1\right)^{1/2} = \frac{V'_{1,z}}{V'_{2,z}} \tag{2.39}$$

- RMS intensity of x- and y- velocity

$$\frac{(3c)^{1/2}}{2} = \frac{V'_{1,x}}{V'_{2,x}} = \frac{V'_{1,y}}{V'_{2,y}} \tag{2.40}$$

The freestream direction in the above expressions is assumed to be along the z-axis, corresponding to the convention followed throughout this work. An important value to characterize in wind tunnel test sections is the freestream turbulence intensity encountered. Experimentally this can be easily done by acquiring freestream velocity measurements in the test section. Due to the presence of the settling chamber (flow conditioners) upstream of the test section, turbulence can be assumed to be isotropic. Under this assumption the square of the time-averaged fluctuating velocity components in the three Cartesian coordinates are assumed equal.

$$(\overline{V'_x})^2 = (\overline{V'_y})^2 = (\overline{V'_z})^2 \tag{2.41}$$

In addition, the cross-flow velocity components can be assumed to be negligible. Knowing this the mean velocity component can be assumed to be equal to the mean velocity in the flow

direction. Combining the previous two assumptions, turbulence intensity can be estimated by acquiring unidirectional (stream-wise) velocity measurements in the center (stream-wise and cross-sectional) of the test section.

$$I \approx \frac{\sqrt{(V_z')^2}}{V_z} \tag{2.42}$$

This expression can therefore be used to obtain an estimate of turbulence intensity in the test section given single-axis measurements. This was performed and shown in Section 2.3.1.2.

Hot wire anemometers are sensors used to measure fluid velocity by exploiting a combination of multiple phenomena in heat transfer, fluid dynamics, and electrical conduction. A heated fine wire which is part of an electrical control circuit is subjected to a fluid flow field. The flow past the wire has a cooling effect thereby affecting the wire's electrical resistance and thus providing input for the control loop trying to maintain a certain variable constant. Different types of hot wire anemometers exist, with the main difference being that variable: Constant Temperature Anemometer (CTA), Constant Voltage Anemometer (CVA), and Constant Current Anemometer (CCA). The sensors used in the current work were CTA.

Resistance of electrical conductors is affected by their temperature. Increased temperature causes atoms making up the conductor to vibrate faster, posing larger resistance to charge-carrying electrons within. The change in temperature is proportional to the rate of change of of resistance and thus a temperature coefficient for resistance is the proportionality constant α. If the change in temperature is relatively small, the expression can be linearized and temperature difference is proportional to the ratio of change in resistance to the initial resistance.

$$\frac{\Delta R}{R_0} = \alpha \Delta T \tag{2.43}$$

A reference temperature T_0 can be set at which the conductor would have a resistance R_0. When the temperature of the conductor changes from that value, the final resistance R can be obtained in terms of the initial resistance R_0, initial temperature, final temperature T, and temperature coefficient of resistance by rearranging the terms in the previous expression.

$$\frac{R - R_0}{R_0} = \alpha (T - T_0) \longleftrightarrow R = R_0 [1 + \alpha (T - T_0)] \tag{2.44}$$

The overheat ratio a can be subsequently defined as follows.

$$T - T_0 = \frac{a}{\alpha_0} \tag{2.45}$$

The values of reference temperature and corresponding wire resistance and temperature coefficient of resistance are provided by the manufacturer. If not, they can easily be measured using a multimeter device. The over temperature of the wire $T - T_0$ is usually desired as 200 Kelvins higher than expected flow temperature (220 Kelvins for air at room temperature). With this a suitable overheat ratio can be chosen. The recommended value for the overheat ratio for air flow is $\alpha = 0.8$.

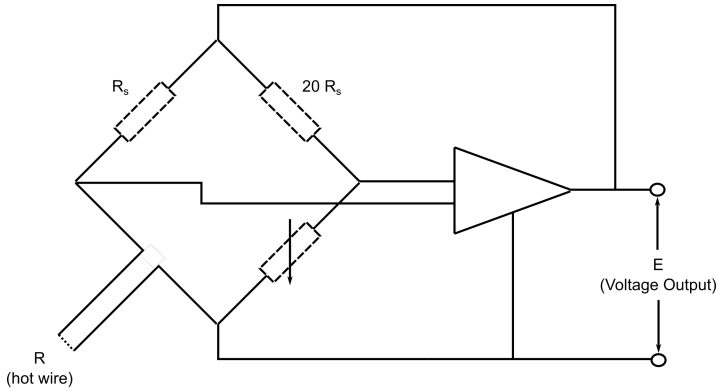

Figure 2.3: Wheatstone bridge circuit used in CTA anemometers.

The hot wire is connected to a Wheatstone bridge circuit. The voltage across the bridge is connected to a feedback control circuit which maintain constant temperature across the hot wire as its temperature varies. The output of the control circuit as shown in Fig. 2.3 is a measure of the air flow encountered by the hot wire. Before operating a CTA hot wire, two balances must be performed for the circuit. The first is for the variable resistance in the Wheatstone bridge adjusting for added resistance by the cables and prongs used to assemble the hot wire. The second is dynamic balancing, performed to determine the cut-off frequency of the circuit and thus the appropriate sampling frequency corresponding to the Nyquist rate to avoid signal aliasing. Both procedures must be performed at the start of each experiment set. After the equipment is set up, the hot wire anemometer must be calibrated. Calibration is performed by taking freestream measurement (without the presence of the model under study), and calibrating the output electrical signal against a reference measurement. In the current work, a Pitot tube located at the inlet of the wind tunnel test section was used for reference measurements for the calibration procedure which was performed at the start of each experiment. The complete procedure followed when operating the CTA sensors in addition to all relevant equations is given by (Jørgensen, 2002).

2.2 Geometry and CAD Modeling

2.2.1 Structure, Dimensions, and Coordinate System

A guyed met mast located in Aboadela, Portugal was chosen as the test case. The mast body is made up of repeating construction units joined end-to-end by flanged connections.

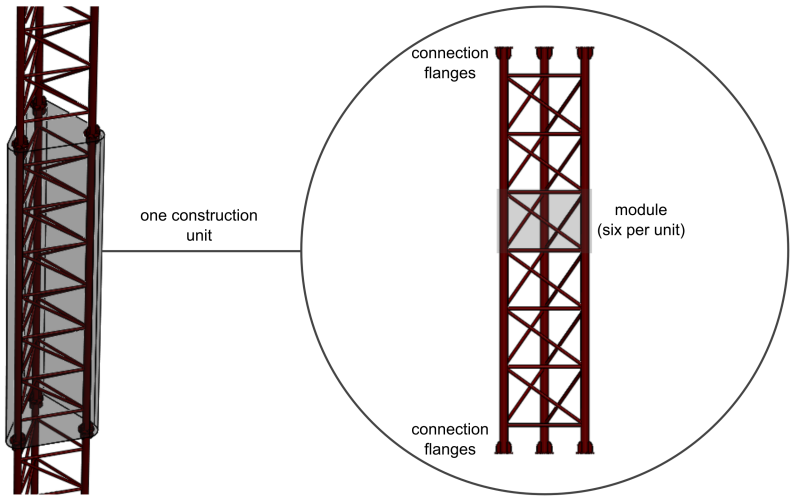

Figure 2.4: Partial view of 3D CAD model made for the mast under study. Construction units and their internal periodic modules are labeled.

The units have a triangular lattice structure made up of three legs (vertical members) interconnected by diagonal and horizontal members; each transverse member welded to two legs. Within each construction unit six identical modules can be identified, each 0.43 meters long. Construction units are 3 meters long and with six modules within, this leaves 0.21 meters at either end where the flanged connection is made to consecutive units. The mast legs and transverse members have circular cross-sections, with external diameters of 60.3 millimeters and 21.3 millimeters respectively, corresponding to standard steel tube sizes. Leg center-to-center distance is 0.6 meters and therefore the mast width viewed horizontally (from any angle) is 0.6603 meters. The above dimensions in addition to other ones relevant to the study are listed in Table 2.1.

Figure 2.5 shows a top view of the mast and coordinate system defined and used as the frame of reference throughout this work. The y-axis is directed out of the page being the vertical axis and coincides with the center axis of the mast, equidistant from the three legs. Incident wind is assumed to have no vertical component and therefore is expressed in terms of speed and (mean) direction on the horizontal plane. Wind at 0° is perpendicular to one of the mast faces, which can be specified arbitrarily due to the geometry's cyclic symmetry, and the angle is measured

Table 2.1: Dimensions of met mast under study.

Dimension	Description	Value
h_m	module height	0.43 m
h_u	unit height	3.00 m
L	leg center-to-center distance	0.60 m
ϕ_l	leg diameter	60.40 mm
ϕ_t	transverse member diameter	21.30 mm
ϕ_m	mast diameter (measured from mast center to leg center)	692.8 mm
ϕ_c	mast diameter (diameter of circle circumscribing the mast)	753.1 mm

counter-clockwise from the z-axis as demonstrated in the figure. An arbitrary location can also be chosen for the origin anywhere along the center axis.

2.2.2 Geometric Properties

The first geometric property to be considered was symmetry. The mast structure can be found to:

- *not* exhibit reflection symmetry, meaning that it is not possible to obtain the same geometry by a reflection about any plane (vertical or horizontal), or equivalently by a rotation of 180° about any axis;
- exhibit *cyclic symmetry* with an angle of 120° about the center axis. This means that a 120° (or any multiple thereof) rotation about the center axis would result in the same geometry. The cyclic symmetry condition imposes that all geometric properties repeat every 120° and can be mathematically defined:

$$\phi_g(\theta) = \phi_g(\theta \pm 120^\circ) \tag{2.46}$$

  where ϕ_g is any variable which is only a function of the geometry's orientation.

Projected area in flow direction is an essential variable to calculate for external flow problems. Since wind direction was considered variable, projected area of the mast is a function thereof. This is demonstrated in Figure 2.7. A Matlab program to calculate projected areas was implemented and works by reading a CAD image capture viewed from the desired angle. Afterwards edge detection is used to locate solid edges and isolate the projected area from the

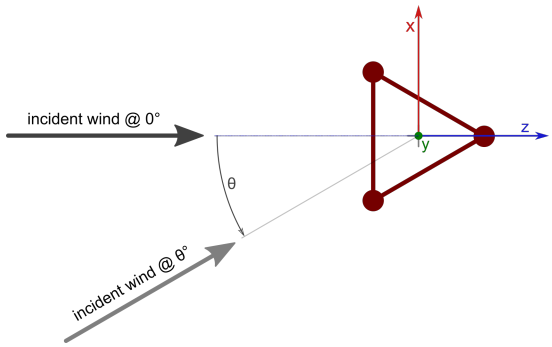

Figure 2.5: Definition of coordinate system used as global reference frame throughout this work.

background. Solidity ratio, defined as the ratio of projected area to the overall envelope area (CEN, 2005), is calculated.

$$t = \frac{A_m}{A_{env,m}} \tag{2.47}$$

Envelope area is independent of incident wind angle since incident wind does not have a vertical component in which case it is equal to module height (0.43 meters) multiplied by module width (0.6603 meters). Given the numerical value of envelope area, the implemented program can therefore determine the solidity ratio and projected area from the input image using Eq. 2.47.

$$t_m = \frac{A_m}{A_{env,m}} = \frac{A_m}{h_m \times w_m} = \frac{A_m}{0.43 \times 0.6603} = 3.522 \times A_m \tag{2.48}$$

Calculations were made for the full 360° circle divided in 10° intervals. The results are plotted in Figure 2.8.

Table 2.2: Calculated projected areas and solidity ratios.

θ	A_m	t_m	θ	A_m	t_m	θ	A_m	t_m
-90	0.0986	0.347	-30	0.0986	0.347	30	0.0986	0.347
-80	0.121	0.426	-20	0.121	0.426	40	0.121	0.426
-70	0.118	0.416	-10	0.118	0.416	50	0.118	0.416
-60	0.117	0.412	0	0.117	0.412	60	0.117	0.412
-50	0.118	0.416	10	0.118	0.416	70	0.118	0.416
-40	0.121	0.426	20	0.121	0.426	80	0.121	0.426
-30	0.0986	0.347	30	0.0986	0.347	90	0.0986	0.347

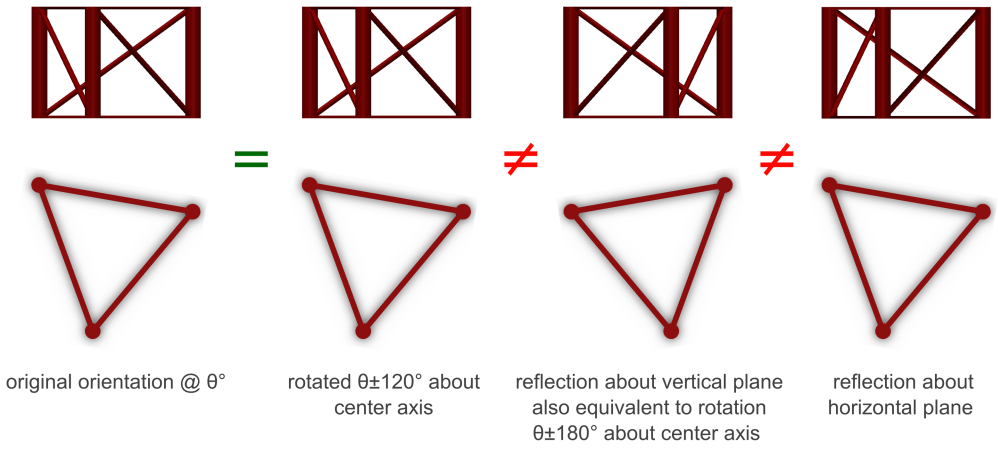

Figure 2.6: Symmetric properties of mast under study.

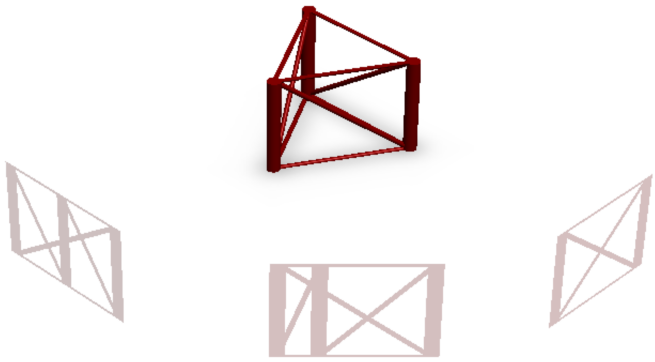

Figure 2.7: Demonstration of different projected areas for varying incident wind angle.

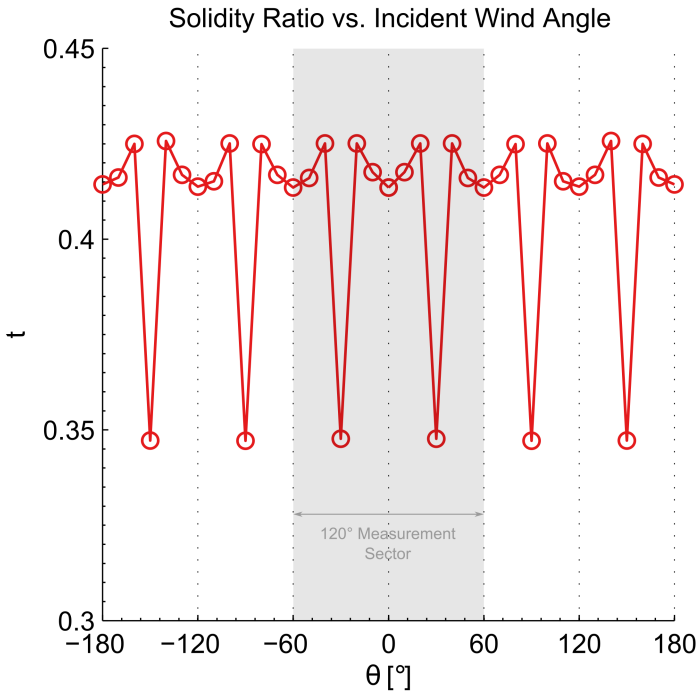

Figure 2.8: Plot of calculated projected areas of a one module vs. different wind directions; highlighted is a 120° measurement sector.

Repetition of values every 60° rather than 120° (as would be expected from cyclic symmetry) is due to the fact that projected area is identical for incident wind from opposite directions ($A_m(\theta = A_m(\theta \pm 180°))$) which also corresponding to a reflection. Although it has been previously shown in Figure 2.6 that planar symmetry is not exhibited since an inverted geometry is obtained instead; however projected area is the same for two inverted areas albeit with different orientation. Combining both relations it can be found that $A_m(\theta = A_m(\theta \pm 60°))$ which is observable in the results. Isolating a 120° measurement sector for the met mast, [-60°,60°], the numerical values are listen in Table 2.2.

Minimum solidity is encountered when two of the mast legs are aligned with the wind direction, occurring at angles {-60° ,-30° ,30° , 60°}. Maximum solidity is encountered when the legs are slightly off, increasing blockage, and occurs at {-40°,-20°,20°, and 40°}.

2.2.3 Simplified Geometry for CFD Analysis

Minute geometrical details are often omitted in CFD analysis. Flanges, bolts, bolt holes, and nuts are all examples of minuscule components which might have infinitesimal effect on the solution yet can significantly enlarge the problem size due to the number of discretization elements needed to model their geometry. There is no strict reference in the field of CFD analysis as to which details should be omitted or modified and this decision is up to the researcher to decide. However, the solution must be confirmed not to be sensitive to those modifications.

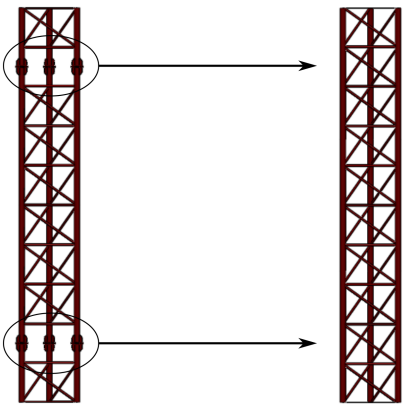

Figure 2.9: Simplification of real geometry for CFD analysis.

In the current work, some geometric details were modified and others omitted for a more efficient CFD analysis. First, connection flanges were omitted. In addition, the triangular lattice

modules were assumed to repeat with no gaps (gaps made connection flanges were omitted). These modifications are demonstrated in Fig. 2.9.

Both alterations are made under the assumption that the final solution will not be affected. This does not necessarily mean that the physical nature of the problem is unchanged, but rather implies that the desired phenomenon can be modeled unaltered; which was verified throughout this work.

2.3 Wind-Tunnel Experiments

2.3.1 LAC Wind-Tunnel Specifications

The LAC (Laboratory of Aerodynamics and Calibration) wind tunnel was used to conduct the required experiments. The tunnel is a blowdown open circuit wind tunnel with a square cross-section closed test section. The tunnel characteristics fit the classification of small, low-speed wind tunnels given by (Mehta and Bradshaw, 1979; Bell and Mehta, 1989).

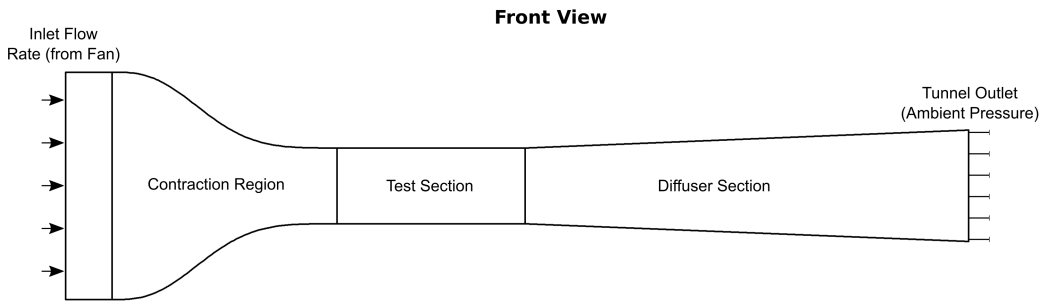

Figure 2.10: Front view of LAC wind-tunnel showing settling chamber, contraction region, test section, and diffuser.

A square cross-section of the tunnel is maintained along the wind flow direction. This means that Fig. 2.10 shows both front and top projections of the tunnel. The figure is drawn with correct proportions (by scaling for a 1 meter-squared test section). Table 2.3 lists the tunnel dimensions.

2.3.1.1 CTA Calibration

Calibration of CTA sensors used in this work was performed according to instructions provided by (Jørgensen, 2002). Two different CTA devices were available. The first was the TSI IFA-100

Table 2.3: Dimensions of LAC wind tunnel.

Property	Value	Property	Value
Contraction Inlet Height	3	Tunnel Outlet Width	1.47
Contraction Inlet Width	3	Tunnel Outlet Area	2.16
Contraction Inlet Area	9	Maximum Test Section Velocity	25
Contraction Outlet Height	1	Fan Inlet Length	0.62
Contraction Outlet Width	1	Contraction Length	2.97
Contraction Outlet Area	1	Test Section Length	2.49
Diffuser Angle	3.25	Diffuser Angle	5.86
Tunnel Outlet Height	1.47	Total Tunnel Length	11.94

CTA which uses a hot wire sensor, with an output corresponding directly to bridge voltage E. To perform velocity calibration, the wind tunnel fan speed was set to $\{0, 10, 15, 20, 25, 30, 35, 40, 45, 60\}$ as a percentage of the maximum fan RPM. For each fan speed, ten minute measurement were made using both the Pitot tube and the hot wire. Fig. 2.11 shows an example velocity calibration performed.

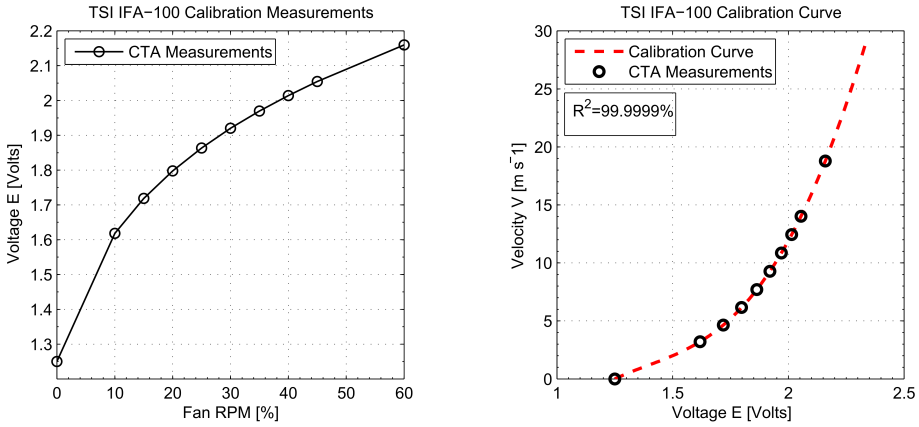

Figure 2.11: Velocity calibration procedure for hot-wire anemometer.

A fourth-order polynomial function is used to fit the obtained measurements and thus acquire a calibration curve for the hot wire. The calibration was repeated at the beginning of each experiment set to account for ambient environment variations.

The other sensor used was ANE02 *, a hot film anemometer. Hot film anemometers have the same theory of operation as hot wires, albeit with a different operating range. Although more sensitive to small velocity fluctuations, the total velocity range and frequency resolution is substantially less than their hot wire counterparts. ANE02 contained an internal signal-conditioning circuit, providing current output ranging from 4 to 20 mA for a velocity range of 0 to 12.5 m/s. Although the circuit is internally calibrated, variations in ambient conditions can affect the response, and

*ANE02 is the LAC reference number.

thus a velocity calibration was also performed at the start of each experiment set in which ANE02 was used. Fig. 2.12 shows an example of the velocity calibration, performed in an identical procedure as the TSI IFA-100 hot wire.

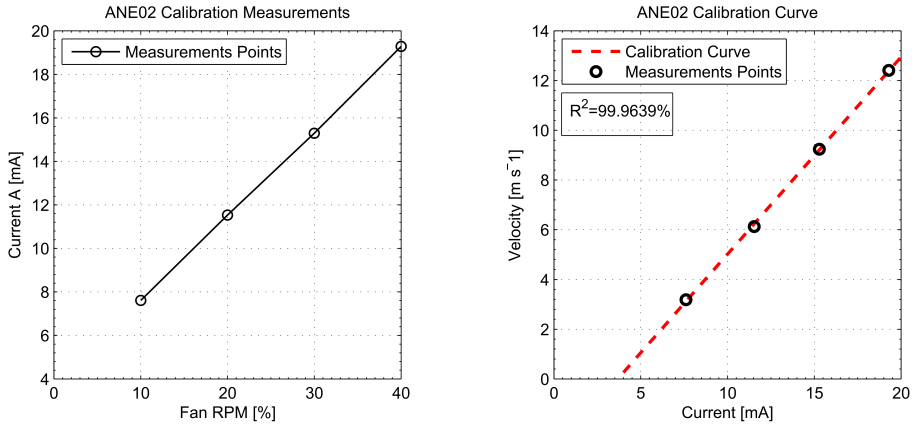

Figure 2.12: Velocity calibration procedure for hot-film anemometer.

2.3.1.2 Test Section Turbulence Intensity

The hot film ANE02 was used to calculate the freestream properties of the wind tunnel used for this work according the procedure explained in Section 2.1.7, which was found to be equal to 0.2%. The measurements are the same used for the velocity calibration procedure explained in the previous section. Fig. 2.14 and 2.15 show the obtained measurements, indicating mean values and standard deviation. Fig. 2.13 shows the probability density function calculated, with the corresponding value of turbulence intensity.

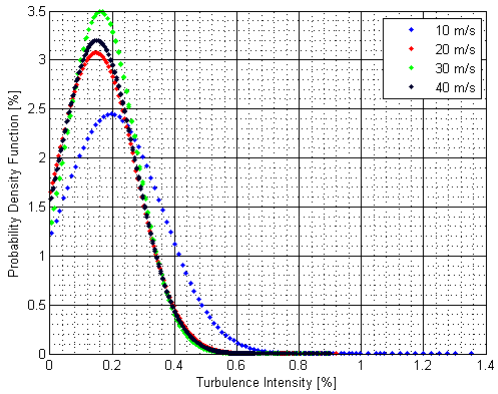

Figure 2.13: Probability density function of turbulence intensity in LAC wind tunnel.

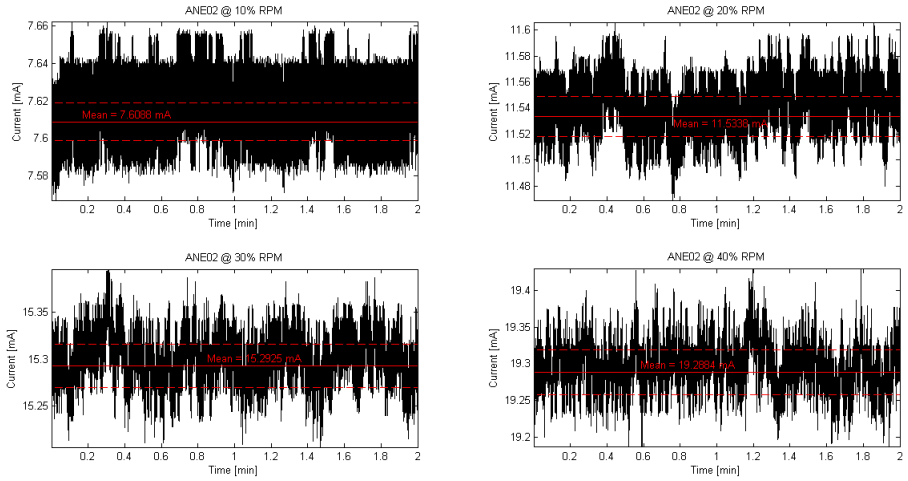

Figure 2.14: Sample of velocity measurements taken by ANE02 for characterizing LAC wind tunnel test section turbulence intensity.

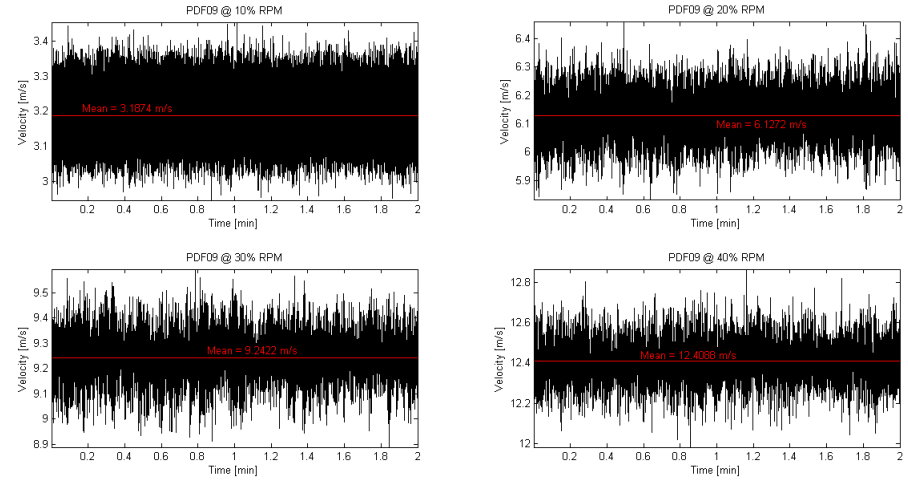

Figure 2.15: Sample of velocity measurements taken by PIT09 for characterizing LAC wind tunnel test section turbulence intensity.

2.3.2 Performed Experiments

Experiments were preformed on a scaled-down model of the met mast under study. The design of the scaled-down model is explained in Section 3.1 as the process contains some preliminary results contributing to the final conclusions made by this work.

2.3.2.1 Experiment Set #1

The first experimental set aimed at investigating the velocity dependency of the flow distortion. Maintaining a constant orientation corresponding to the default orientation (0°), test section freestream velocity is varied along the tunnel fan operating range. ANE02 was used to take measurements 23 millimeters along the negative x-axis (on the right side of the mast from the wind direction). This experiment was performed primarily to test the speculation made that mast distortion effects are wind speed-independent. It would also give insight on similarity conditions of the problem from the scientific perspective, as well as self-similar properties of turbulence. To minimize its interference effects, the probe was fixed to the test section wall rather than the model itself.

The results of this experiment set are presented in Section 3.3, and were also used to validate the CFD model used in addition to the appropriate turbulence model.

2.3.2.2 Experiment Set #2

Having tested the velocity dependency of the problem, another experiment set was performed to investigate that of wind direction. Measurements in this experiment were taken using the TSI IFA-100 CTA, located 50 cm downstream of the mast model. Measurements were taken for angles of 0°, 10°, 20°, 30°, 40°, and 60°. To obtain a comprehensive parametric study, the wind speed was also varied for each angle.

Due to signal contamination problems, this experiment set was discarded from the current work, and CFD results were used solely to investigated angular dependency.

2.4 Computational Fluid Dynamics

In this study CFD simulations were viewed as the main tool of analysis. Indeed, the main objective of wind tunnel testing was to validate the numerical models used in CFD analysis. Once an appropriate numerical model is constructed, all defined variables of interest can be analyzed and subsequent conclusions drawn. Perhaps one of the most valuable outcomes of this work is establishing the guidelines for CFD modeling of the problem at hand, something which has been found lacking in the conducted literature review. This is due to arbitrary values set for many definitions of the CFD models (boundary conditions, computational domain size, etc.) in previous literature when modeling the problem.

This work thoroughly investigated different parameters in order to reach the most consistent method of CFD modeling which is capable of simulating the real problem. Such parameters include the grid type to be used, turbulence modeling, and computational domain size. The latter involves determining the effect of increasing number of modules in the representative section and thus increasing the domain size. An important follow-up is a a question raised and subsequently answered by this work, which has not been found previously considered in literature: Should the turbulent boundary conditions be a function of domain size? and if so, does freestream turbulence have a physical effect on the problem at hand? As all those factors contribute to the final outcome of this work, relevant studies are presented in 3.

This section describes the construction of the computational domain and grid type, in addition to grid independence studies.

2.4.1 Computational Domain and Grid Type

A circular boundary is set to appoint the far-field freestream conditions. The size of the boundary should be as small as possible to minimize the computational time of the simulations; yet it must be large enough such that it does not have any effect on the solution. Two factors can used to evaluate this. The first is blockage effects, as was the case with wind tunnel experiments. Information provided by Annex G of (IEC, 2005) can also be used. Since the interference effects of the mast can extend up to a very long distance to entirely dissipate, a limit of acceptable accuracy needs to be as to where they are considered fully decayed. At a distance of 10 mast leg distances upstream of the mast, the distortion error falls below 0.2% (IEC, 2005). The inlet and outlet boundaries were therefore located at a distance of 7.5 meters from the center of the mast. This is equivalent to 10 times the circumferential radius (refer to Table 2.3) of the mast and over 12.55 mast leg distances, to absolutely ensure that adequate distance has been kept to avoid the boundaries affecting the solution.

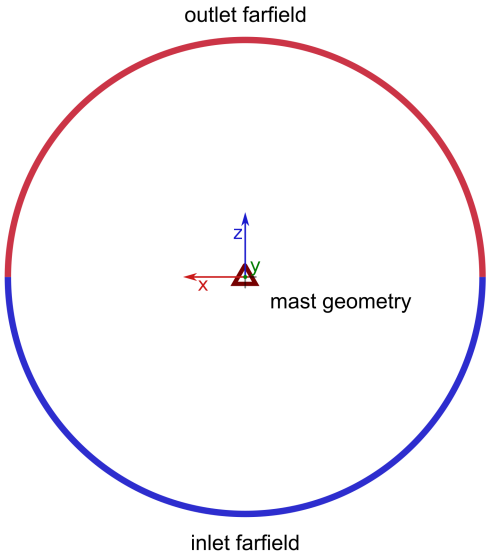

Figure 2.16: Top-down view of proposed computational domain showing inlet and outlet farfields, mast location, and reference coordinate system.

Setting the vertical size of the domain involved the same problem as with the design of the scaled-down wind tunnel model (refer to Section 3.1). The mast geometry is set to span the entire vertical spacing of the domain, ending at both top and bottom boundaries. Given that enough number of modules have been included in the model to establish periodicity effects, those boundaries can be set to symmetry conditions (which is equivalent to a slip or zero-shear wall). Different number of modules, and therefore different vertical sizing, of the domain is used for different studies depending on the output in question. For all cases and studies, velocity results are analyzed at a horizontal plane located in the center of the model as with the initial periodicity study. This is done to obtain values least affected by the boundary conditions (refer to Fig. 2.17).

Having proposed a computational domain for the problem, the next step was to determine the meshing approach to properly discretize the domain. Fully structural grids are almost always preferable in CFD analysis in terms of both accuracy and efficiency. However, due to the complex geometry of the lattice structure of the mast comprised of tight geometric features existing at intersections of the mast members and legs, obtaining a fully structured mesh would be a very complex task, and was eminently out of the scope of this work.

A second-best alternative has been proposed: a hybrid grid consisting of two blocks. This approach was found to be commonly used in similar flow problems, when regions of the flow volume have geometries which are too complex to be efficiently discretized by a structured grid. For the volume of fluid in the direct vicinity of the mast (i.e., inner flow volume). A fully structured grid was used for the volume beyond this inner region extending to the far-field boundaries (i.e. outer flow volume). An interface region (cylindrical surface) exists where both

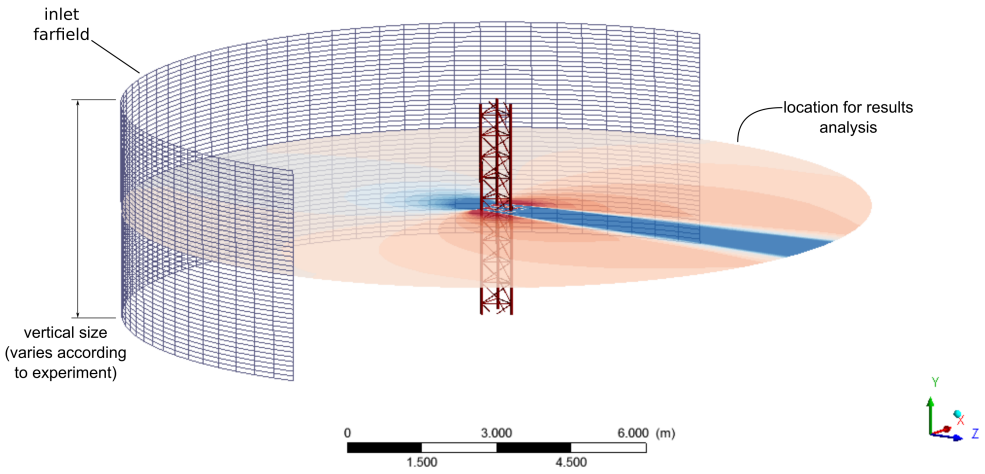

Figure 2.17: Partial three-dimensional view of computational domain highlighting vertical sizing and location at which results are analyzed.

regions meet. Although hybrid grids can be non-conformal (i.e., no alignment of grid lines and therefore existence of some hanging nodes at block interfaces), conformal meshes are always preferable for an accurate solution (Bern and Plassmann, 2000). A conformal mesh was imposed by the mesh generator and was achieved for all grids used.

Discretization has a significant impact on solution accuracy and validity. Five important properties should be verified when using a numerical method: consistency, stability, convergence, conservation, boundedness, and are grid-independence and solution stability. This study aims to verify whether the obtained solution is independent of the discretization. In other words, the grid refinement level is varied (usually with a factor of 2 or $\sqrt{2}$ as a best practice guideline) and the solution is compared for the different grid spacings. A grid-independent solution is one which converges to a certain value, that of the differential equations (given the grid is consistent). A grid dependency test was performed prior to CFD experiments of the mast. Subsequent grid refinements are made with a $\sqrt{2}$ factor. The grid sizes are presented in Table 2.4.

The first measure taken was the drag coefficient on the mast walls. Fig. 2.19 shows monotonic convergence of drag coefficient for both unstructured and hybrid grids. The hybrid grid can be seen to achieve better convergence. This is expected due to the structured grid alignment with the flow gradients. Fig. 2.20 and 2.21 show velocity profiles up and downstream of the mast, in addition to the sides. The results clearly show convergence of both grid types, with the hybrid grid exhibiting better convergence, especially in the downstream of the mast. Therefore, the results show that the obtained solution for all flow variables is indeed grid-independent.

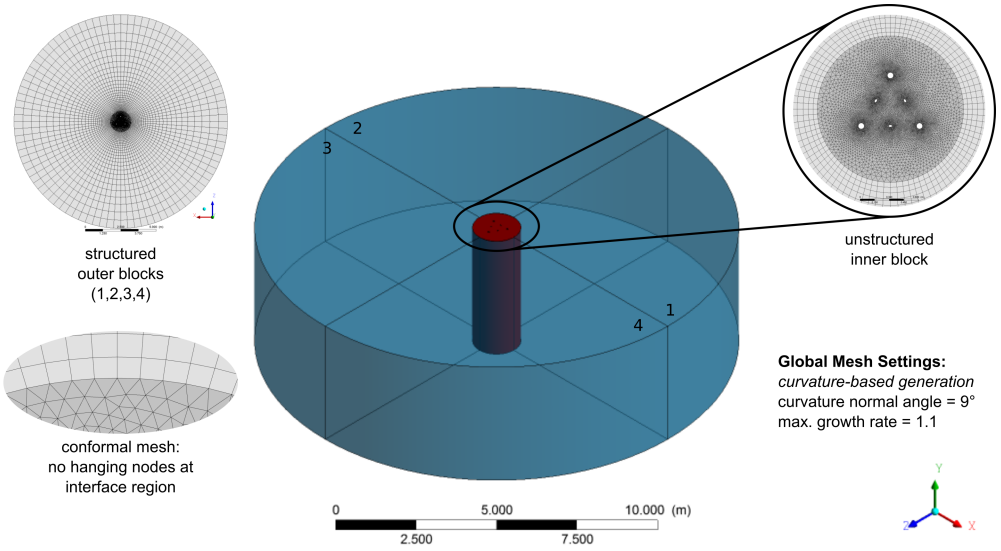

Figure 2.18: Construction of hybrid grid showing four blocks, conformal interface region, and a top-down view of generated grid.

Table 2.4: Mesh sizing parameters used for grid independence study.

		Grid Refinement			
		I	**II**	**III**	**IV**
Size Parameters	**Min Size [mm]**	12.7572	9.0207	6.3786	4.5104
	Max Face Size [m]	1.2757	0.9021	0.6379	0.4510
	Max Size [m]	2.5514	1.8041	1.2757	0.9021
Grid Size ($x10^6$)	**Unstructured**	1.0796	1.8481	3.2848	5.5148
	Hybrid	0.9251	1.6531	3.0622	5.2518

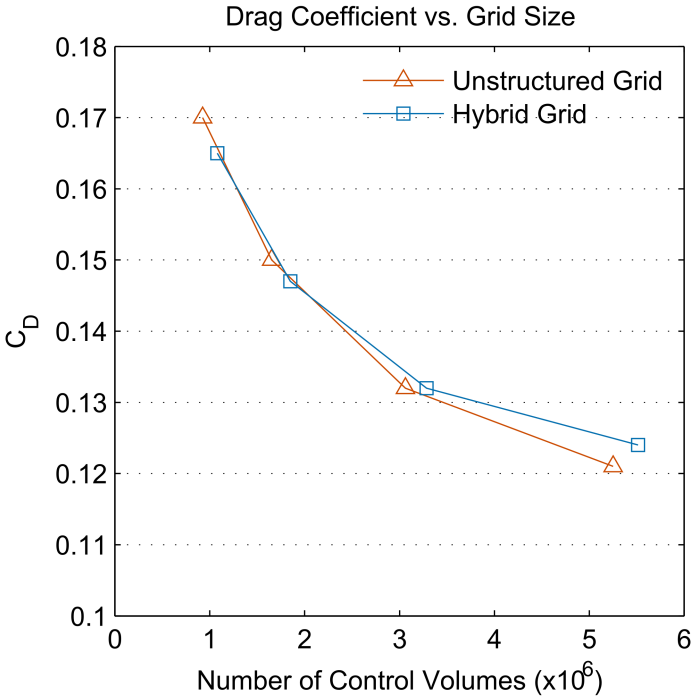

Figure 2.19: Convergence of drag coefficient showing grid-independence for hybrid and unstructured grids.

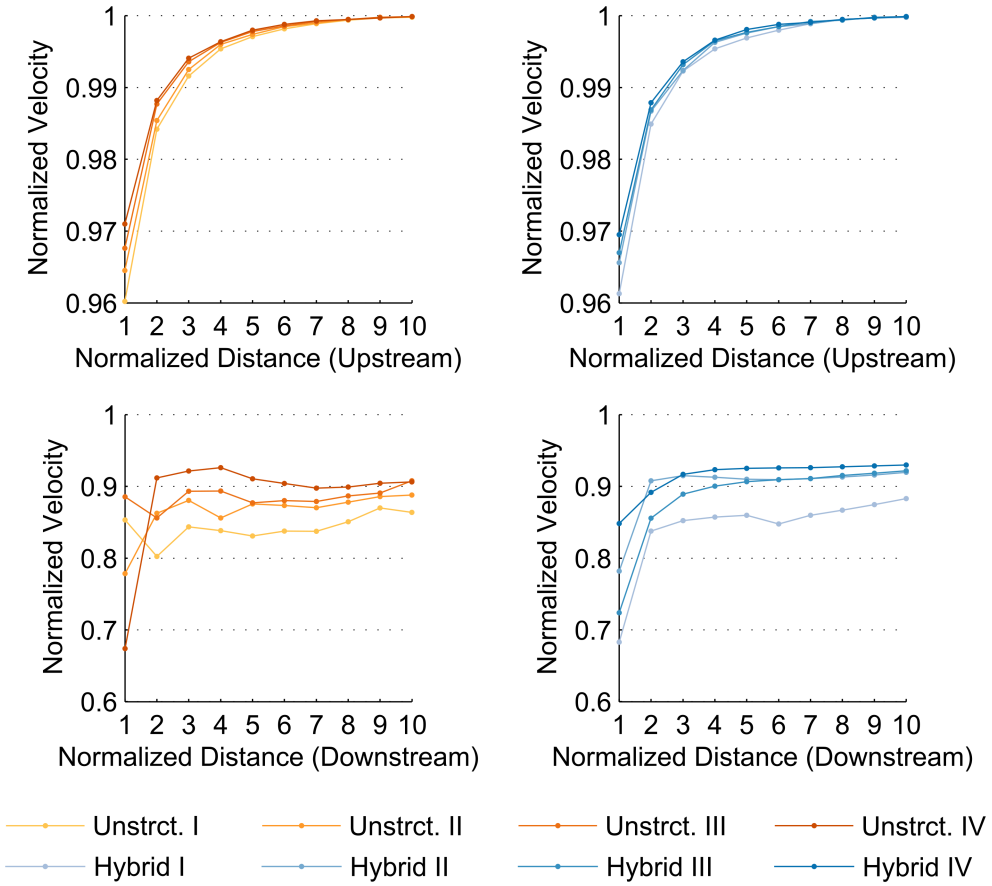

Figure 2.20: Convergence of velocity profiles up and downstream showing grid-independence for hybrid and unstructured grids.

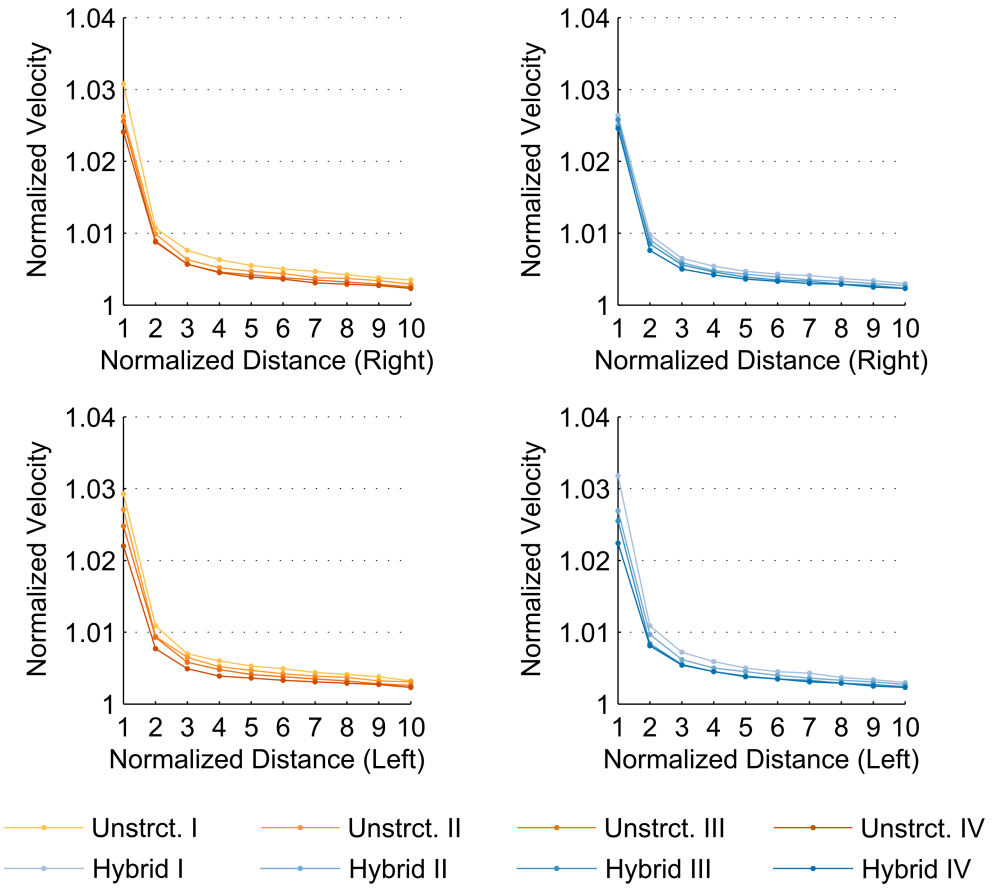

Figure 2.21: Convergence of velocity profiles on the sides showing grid-independence for hybrid and unstructured grids.

Chapter 3

Results

The first section of this chapter (Section 3.1) explains the design process for the scaled-down model of the mast. Each factor contributing to the design is studied separately and resulting constraints from each are compiled to obtain a final design problem. Although this constitutes of the methods used to perform the final investigation, the results obtained throughout the process contributed to the final conclusions. Therefore the first section could be considered to provide preliminary results for the problem at hand.

After fully defining methods used to perform both CFD and wind tunnel experiments, in addition to preliminary CFD results, the following sections each investigate a separate variable contributing to the problem

The influence of freestream turbulence is investigated in Section 3.2. Different approaches of setting freestream turbulence boundary conditions used by previous studies are compared with ones proposed by the current work; and the appropriate boundary conditions to be applied in the CFD models were determined. The numerical model used was then validated in Section 3.3 by comparison with measurements taken in the wind tunnel using the scaled-down model. In Section 3.4, the validated CFD model is used to simulate flow conditions at different heights of the mast with freestream conditions along the atmospheric boundary layer. Finally, the effects of incident wind angle are studied for both a triangular and square lattice mast in Section 3.5.

All results presented throughout this chapter are obtained by probing on four different locations corresponding to upstream (negative z-axis), downstream (positive z-axis), and sides left and right (x-axis) of the center module (refer to Fig. 2.16). The sampling locations are separated by multiples of the mast leg distance to correspond with normalized distance (R/L) in (IEC, 2005).

3.1 Design of Scaled-Down Model

To perform wind tunnel experiments, a scaled-down model of the met mast was needed, capable of replicating the full scale flow distortion. The four factors influencing the design of the scaled-down model are:

1. flow periodicity,
2. wind-tunnel specifications,
3. scaling effects, and
4. manufacturing limitations.

Investigating each factor separately resulted in different constraints forming the input of a design problem. Each study is presented in the following subsections, followed by the design solution obtained by optimizing the best dimensions which satisfy the constraints and maximize the benefits.

3.1.1 Flow Periodicity

For CFD simulations and wind-tunnel experiments alike, modeling the entire mast is not practically possible due to obvious reasons. Scaling down the entire geometry to fit in a wind-tunnel test section would be associated with a very high scaling factor and a representative section (a given number of modules) should be used instead. To determine this number of modules which would be sufficient to replicate the flow regime around the entire mast, a flow periodicity study was performed. The met mast is made up of repeating identical modules and as a result of such geometric periodicity, the flow distortion is in itself anticipated to be periodic along the vertical axis.

This flow periodicity is disrupted by discontinuation of the geometry which results from a physical boundary (earth, wind-tunnel walls, mast top, etc.) or a non-physical one in the case of CFD simulations (computational domain boundary conditions). A region of non-periodic flow is expected adjacent to the boundary. The first CFD study performed in this work aimed at investigating this flow periodicity and determining the number of modules within the non-periodic flow region. This would therefore provide the total number of modules needed to establish periodic flow. Since the aim was was to design the scaled-down model at an early stage of the work and was the first, this CFD experiment was performed following similar

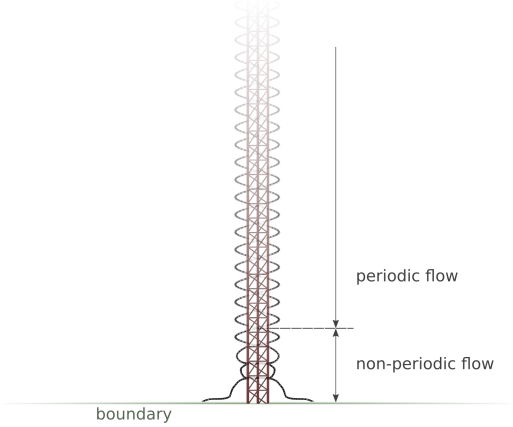

Figure 3.1: Demonstration of flow periodicity and its disruption near the boundaries.

methodology to that of previous literature. Later stages of this work presented in the following sections performed a rigorous CFD study investigating various numerical aspects and confirming the validity of the model used in this study. Although it was later shown that the current method of setting turbulence boundary conditions might be in question, the periodicity of the flow field and therefore the resulting number of modules needed were unchanged. This can be seen by comparing Fig. 3.2 with Fig. 3.9.

Five different computational models were constructed, each containing a number of modules ranging from one to six. The computational domain is shown in Fig. 2.16 with semi-cylindrical inlet and outlet far fields. The $k-\epsilon$ turbulence model was used. Inlet and outlet velocity and turbulence intensity boundary conditions were chosen in accordance with (Fabre et al., 2014). Hydraulic diameter (of the mast frontal geometry) was specified at the boundaries for turbulence spatial properties as listed in Table 3.1.

Table 3.1: Values of hydraulic diameter used for different number of modules included in the geometry.

Number of Modules	Hydraulic Diameter
1	0.7659
2	1.381
3	1.885
4	2.307
5	2.664
6	2.97

The simulations were run and the results obtained were post-processed by calculating the drag

coefficient of the middle module for each model in order to compare the models using a non-dimensional variable. The drag coefficient C_D defined as follows (Schlichting, 1968).

$$C_D = \frac{F_D}{\frac{1}{2}\rho V^2 A} \tag{3.1}$$

Table 3.2: Results of first CFD periodicity test showing drag coefficient (at middle module) change with increasing number of modules considered in geometry.

Number of Modules	**Total Drag Force [N]**	**C_D**	**Percentage Change [%]**
1	10.12	0.627	-
2	12.56	0.779	24.2%
3	13.08	0.811	4.1%
4	13.41	0.831	2.5%
5	13.65	0.846	1.8%
6	13.69	0.849	0.4%

The results are shown in Fig. 3.2. It can be seen that having a total of more than 3 segments is enough to replicate the behavior of many more. In addition it is also proven that very marginal difference is observed beyond five segments. This is an important conclusion to make since it proves viable the assumption made when excluding the the flanges and corresponding gaps. Since each unit has six modules, periodicity is already established within the units and therefore excluding the flanges and their gaps will not have an effect on the middle modules.

By further inspecting the results obtained from the fifth computational model (containing a number of five modules) to calculate the drag coefficient for each of its segments the results are shown in Fig. 3.3, it is shown that close to the boundaries, significant distortion is present. However, the middle modules are seen to have established the periodic flow pattern. The conclusions made by this study are that modeling more than four segments would be sufficient to replicate the flow pattern for the entire mast.

Table 3.3: Result of first CFD periodicity test showing change in drag coefficient along representative section for the case of five modules included.

Module Number (counting from bottom)	**Drag Coefficient**	**$100 \times C_d/C_{d,3}$**
1	0.755	0.51
2	0.823	0.016
3	0.825	-
4	0.827	0.014
5	0.755	0.51

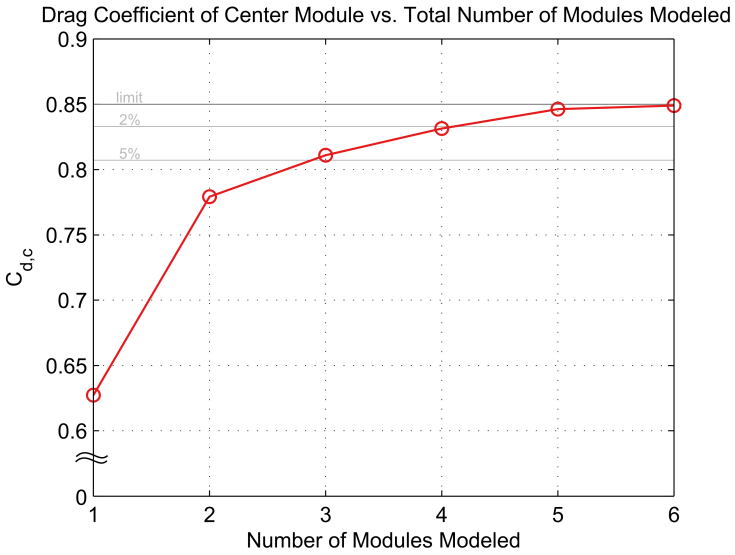

Figure 3.2: Demonstration of flow periodicity with convergence of drag coefficient at middle module for increasing number of modules in the modeled representative section.

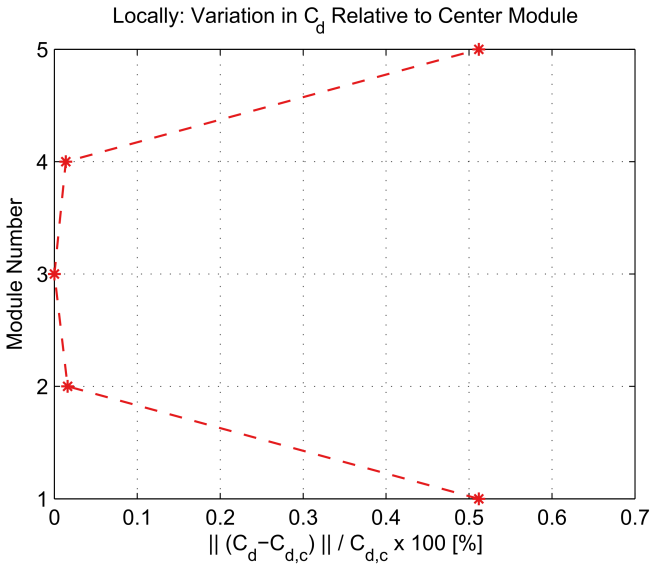

Figure 3.3: Values of drag coefficient for each module given a representative section with five modules included. Boundary effects are seen as a drop in drag coefficient for modules at the extremities of the representative section.

3.1.2 Wind-Tunnel Specifications

The second set of constraints posed on the design of the scaled-down model are due to the wind tunnel specifications which have been listed in the previous section. Since the scaled-down model should be a representative section of the full mast, the section should fit within the tunnel test section, touching top and bottom ends; i.e., the representative section to be scaled-down needs to have a total height of 1 meter. The proposed placement of the scaled-down model inside the test section as shown in Fig. 3.4.

In addition, an offset distance needs to be included the top and bottom of the model for installation purposes and to allow for some space to avoid the test section walls boundary layer; although some CFD analysis performed has shown that it is order of millimeters and as would therefore cause marginal difference.

In addition, blockage effects need to be accounted for. This is of particular importance for experiments performed in closed test sections, where the blockage caused by experimental models can reversibly affect the flow upstream if it is large enough. Many published studies like (Patil and Tiwari, 2008) have concluded that blockage ratios need to be maintained below 10% (and preferably at 5%) for blockage effects not to affect the experiment. The blockage ratio is defined as the ratio of projected area of the model to the test section cross-sectional area.

$$b = \frac{A_p^s}{A_{ts}} = A_p^s \tag{3.2}$$

The final constraint posed by the wind tunnel is its wind speed operating range. The maximum velocity achievable in the test section is roughly 30 m/s. However, instrumentation ranges and safety considerations brings this down to 20 m/s. The minimum measurable wind speed by the measurement devices used is 0.5 m/s.

3.1.3 Scaling Effects

Scaling effects play a vital role in all experimental fluid dynamics studies. Similarity needs to be defined between the fluid flow in both full scale and scaled-down cases. (Barlow et al., 2011) have used the assumption that the leg diameters can be used as the characteristic length of the mast, and Reynolds number based on it can be used. This assumption is based on this problem being an interaction of multiple cylinders in cross-flow; and thus given adequate spacing between the cylinders (i.e., low solidity ratio), the flow fields around each cylinder can be assumed not to interact with one another.

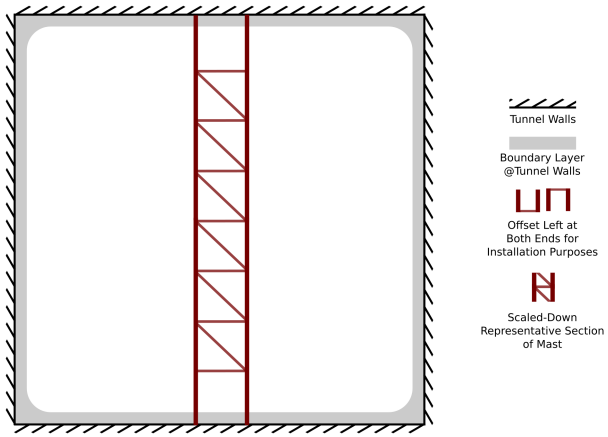

Figure 3.4: Schematic of proposed model placement inside wind tunnel test section.

This was not expected to be a major problem for two reasons. First, as is yet to be shown, this is a turbulent flow problem. The self-similar nature of turbulence implies that the resulting normalized flow fields will be the same for different velocities, given that the incompressibility condition holds. Second, (IEC, 2005) has stated that velocity variation has minimal effect on the flow distortion effect. Although verifying this statement is in itself a current objective, at this stage one can at least assume that the scaling effects will not be big enough to cause major difference and can confidently use any (valid) assumption. Since no better method was available, the assumption by (Barlow et al., 2011) was used to consider the scaling effects.

This changes the current problem to a problem of external flow around an array of cylinders and the scaling effects will be considered, initially, in accordance. Reynolds number is defined for cross-flow around a cylinder (refer to Eq. 3.1).

Since the different diameters of the legs and transverse members would result in different Reynolds numbers, both can be considered to establish a velocity scaling relationship. The smaller diameter would result in a smaller Reynolds number. Since at this stage of the work it is required to know the limitations and constraints on the design of the scaled down-model, the similarity relationship in itself is not required, but rather lower and upper limits resulting from thereof. In other words, a relationship between the scaling factor and the resulting full-scale velocity range being simulated is of interest. The scaling of the mast has to be done in such a way that the entire full-scale operating wind speed range is being considered. This work being primarily focused on wind energy applications, a good way of identifying this is by referring to the (IEC, 2005) standard. Information is provided on the power output of wind turbines by means of field measurements from two separate databases. By looking at Fig. 3.5 it can be seen that quality of measurement for velocities greater than 20 ms^{-1} is of no practical value, since there is a saturation followed by a drop in the power output. the saturation in fact occurs

earlier, around 15 m/s. Therefore the operation range of the mast in full-scale can be assumed to be from 2 ms^{-1} up to $15-20$ ms^{-1}.

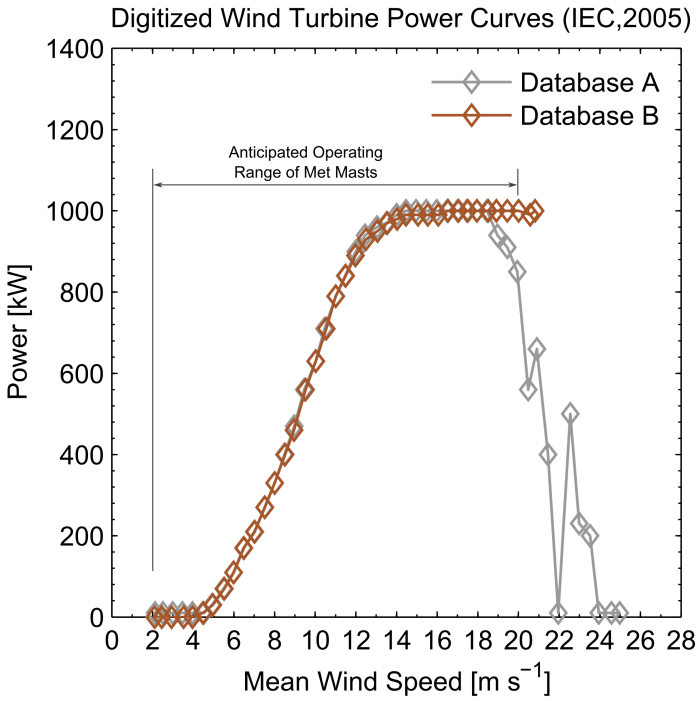

Figure 3.5: Power output of wind turbines as provided by IEC 614200-12-1.

3.1.4 Manufacturing Limitations

The scaled-down model was to be constructed as a welded structure. The members of model would be steel tubes, cut to achieve the appropriate dimensions. Therefore, the final factor affecting the scaled-down model design are manufacturing limitations. Industrial standard steel-size tubes come in external diameters of {10.2, 12.0, 12.7, 13.5, 14.0, 16.0, 17.2, 18.0, 19.0, 20.0, 21.3, 22.0, 25.0, 25.4, 26.9, 30.0, ... 139.7}. Therefore, determining the appropriate scaling factor would involve considering that the diameters of the members would have to be within that range. This is due to thin thicknesses of tubes with small diameter which would make machining operations such as turning inefficient. In addition, a slight distortion of the geometry would have to be performed in order to accommodate for available steel tube sizes.

3.1.5 Design Problem

The design problem involves identifying the solution space determined by the constraints. The resulting design space is shown in Fig. 3.6, with highlighted regions being excluded due to the

inequality constraints applied. The solution space would therefore be the region outside of those excluded areas, which includes candidate values which would provide a design abiding by all posed limitations. Those are listed in 3.4. The problem is now an optimizations problems. More specifically, the choice needed to be made on the number of modules to be included, which would maximize the full-scale wind speed being modeled and minimize blockage effects; all while taking into consideration manufacturing limitations. A choice of 5 modules (third row in the table) was made.

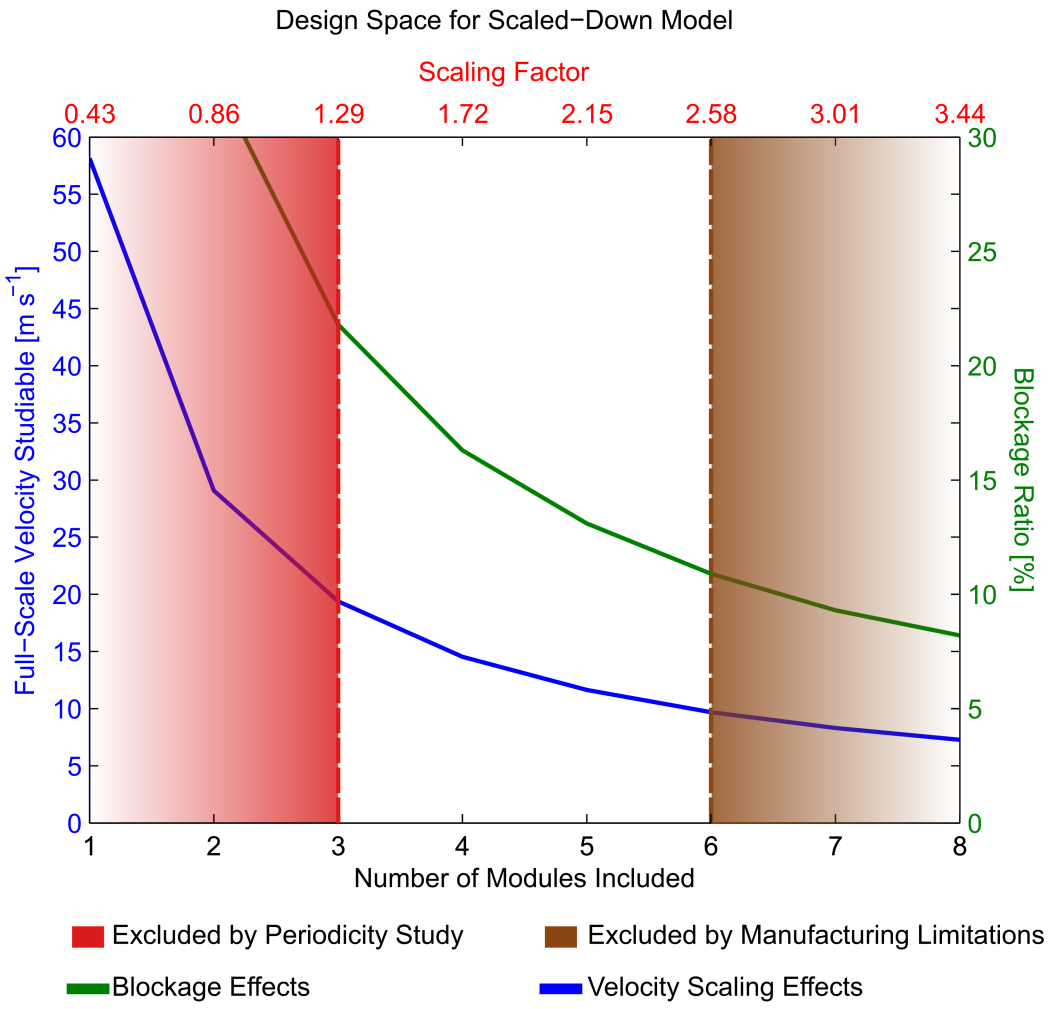

Figure 3.6: Design space for scaled-down model.

3.1.6 Scaled-Down Model

With the decided scaling factor (2.15), the corresponding member diameters would not correspond to commercially available steel tubes. Therefore the dimensions had to be slightly modified to match manufacturing limitations posed. The leg diameters used were 20 mm, while

Table 3.4: Final candidates for the scaled-down model and the final selection (5 modules).

# of Modules	Scale Factor [m^{-1}]	Min. BR	Max. BR	Max. Wind Speed [%]
3	1.29	17.8	21.8%	19.38%
4	1.72	13.3	16.3%	14.53%
5	2.15	10.7	13.1%	11.63%
6	2.58	8.9	10.9%	9.69%

the transverse member diameters were 8 mm. In addition, base plates had to be added to the design to facilitate installation in the wind tunnel test section. Those are shown in Fig. 3.7.

Figure 3.7: Base plates added to facilitate installation in wind tunnel.

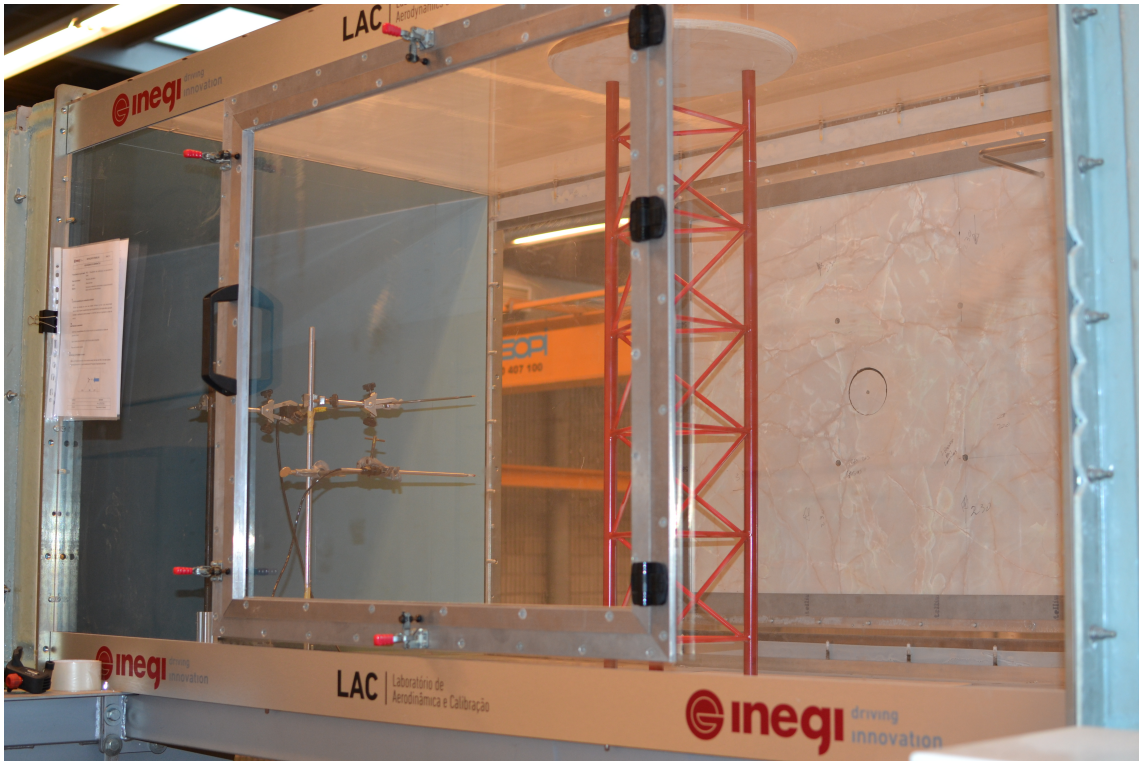

Figure 3.8: Scaled down model assembled and installed in the LAC wind tunnel test section.

3.2 Freestream Turbulence Effects

Setting appropriate turbulence boundary conditions for the CFD simulations was vital for two main reasons. First, the influence of freestream turbulence on flow distortion effects of lattice masts was in itself defined as an objective of this work. Second, the conducted literature review has shown that no common approach was used to consider freestream turbulence values in previous studies. The choice of turbulence boundary conditions was made by comparing three different proposed methods. The first was based on the approach used by (Fabre et al., 2014). It constituted estimating the freestream turbulence intensity encountered at 10%. The turbulence length scale was set proportional to the computational domain (10% of relative inlet height). When comparing to values of turbulence intensity and length scale as given by atmospheric boundary layer profiles presented in Section 2.1.6, some remarks were made. An ideal case of an atmospheric boundary layer was assumed as follows corresponding to the values in Table 3.5.

Table 3.5: Values assumed for ideal ABL profile, satisfying a condition of $V(55\text{ m}) = 10\text{ ms}^{-1}$.

Property	Value
V^*	0.563889
y_0	0.03
δ	1000
κ	0.4237

The values were assumed with the intention of obtaining a velocity of 10 ms^{-1} at an elevation of 55 meters. The only exception was in the case of (Palma et al., 2008), where the velocity was slightly lower. Although the parameters could be changed to obtain the exact velocity only when using the aforementioned theory, it was decided to use the same parameters for all as to maintain consistency.

Table 3.6: Comparison between freestream turbulence parameters at $y = 55$ with different ABL profile theories.

	ABL Profile Theory		
	(Palma et al., 2008)	(Eidsvik, 2008)	(Richards and Hoxey, 1993)
$V(y = 55)$	9.8732	10	10
$I(y = 55)$	8.0883	7.9436	8.406
$l(y = 55)$	21.185	22.0218	23.3035

The approach of (Fabre et al., 2014) set the variables as a function of the computational domain size. This meant that the choice of the number of modules in the representative section not only affected the periodicity (refer to the previous section), but would also have an influence on turbulence boundary conditions, namely the turbulence length scale (velocity and turbulence

intensity were estimated as constants). To compare the resulting boundary conditions of this approach with the more (realistic) values given by ABL profile theories, Table 3.7 shows values of length scale given different domain sizes (i.e., number of modules in representative section).

Table 3.7: Freestream turbulence length scale variation with computational domain size using the approach of (Fabre et al., 2014)

Number of Modules	$l_\infty = 0.1 \times h_s$
1	0.43
2	0.86
3	1.29
4	1.72
5	2.15
6	2.58
10	4.3

It can be seen that even with 10 modules being modeled (very computational inefficient), the value of the length scale is still significantly underestimated (4.3 m) compared with what one would encounter in a real case of atmospheric flow (third row in Table 3.6). This begged the question of whether this difference would influence obtained results, and thus a periodicity study was performed for confirmation. Different geometries with number of modules included ranging within $n = \{1, 2, 3, \ldots 6, 10\}$ were considered. Three different proposed methods for setting the boundary conditions were compared:

1. **ABL:** boundary conditions were set according to what would be encountered in a real life boundary layer. The values were the same for all considered number of segments.

2. **Fabre (scaled with size):** boundary conditions were set according to the same methodology followed by (Fabre et al., 2014), with the length scale being correspondingly scaled with increasing number of modules (and thus relative inlet height).

3. **Fabre (constant):** same as the previous however the values were kept constant and equal to the case of one module being modeled. The purpose of this was to investigate the effect of scaling the length scale with the computational domain size and its effect on the solution.

As the turbulence model to be used is yet to be determined (next section), the $k-\epsilon$ model was used to conduct the current experiments. This is due to the fact that to conduct a proper turbulence sensitivity study, the correct turbulence boundary conditions need to be set.

Fig. 3.9 shows the variation of drag coefficient of the mast section with the number of modules included. The turbulence boundary conditions can be seen to have a significant effect. Also, it

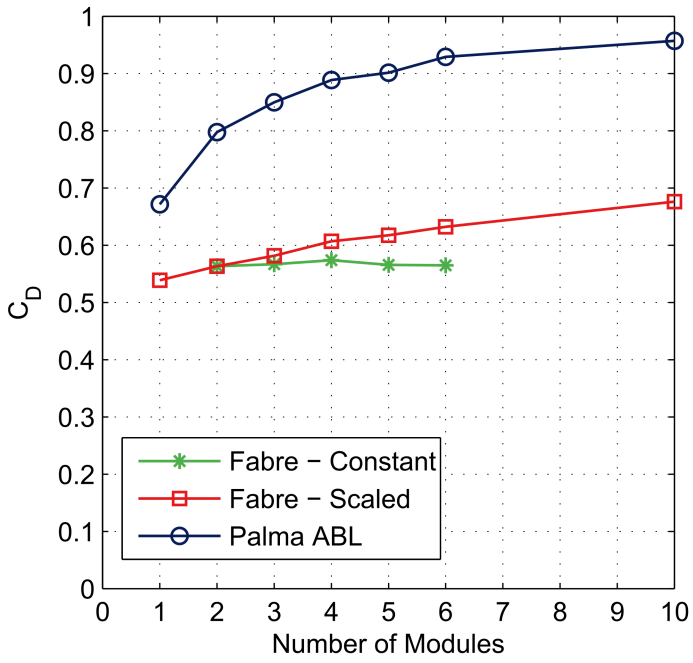

Figure 3.9: Drag coefficient variation with increasing number of modules for different turbulence boundary conditions.

can be seen that scaling the length scale proportional to the domain size alone does not have as significant of an influence, and produces almost the same results.

Fig. 3.10 shows normalized velocity values upstream of the modeled section. The approach of (Fabre et al., 2014) results in less velocity deficit values compared with ABL profile theories. Once again, scaling the turbulence length scale with domain size has no significant effect. However, by comparing the velocity deficient values with the ones given by IEC, one realizes that the results obtained by the method of (Fabre et al., 2014) are closer to IEC than setting them according to ABL profile theories. This is due to the fact that freestream turbulence was not considered altogether in IEC.

The same effect is seen with velocity values on the side of the mast by inspecting Fig. 3.11. In addition, by comparing both results upstream and on the sides, one notices that the freestream turbulence effects are encountered more intensely closer to the mast, and converge to one another (and to IEC) further from the mast center, which was anticipated.

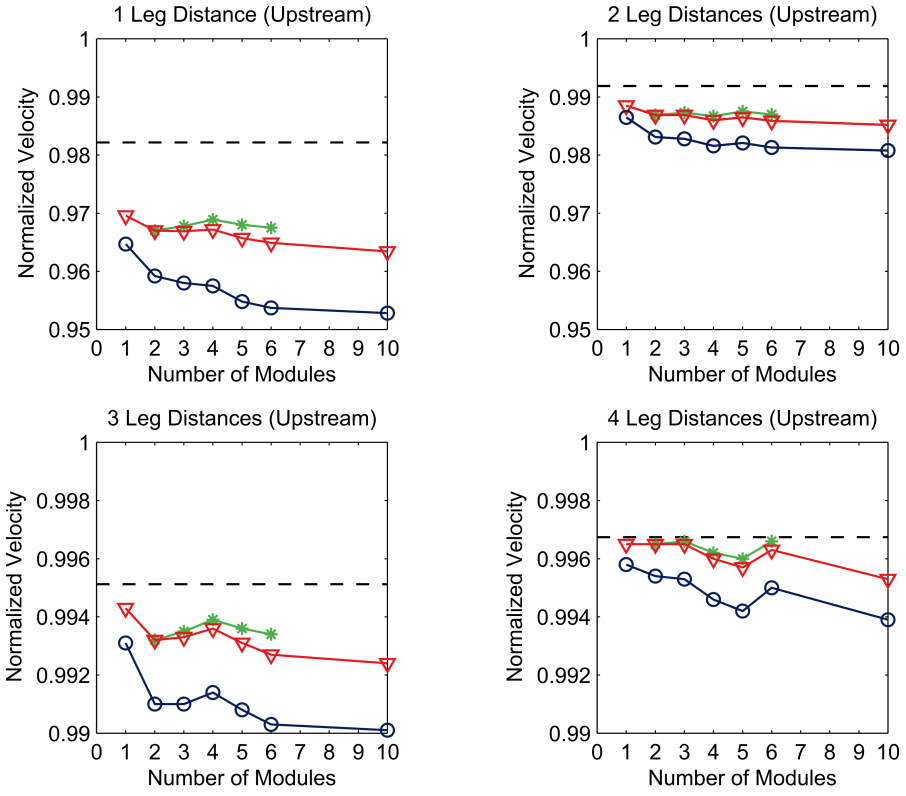

Figure 3.10: Upstream normalized velocity profile for different turbulence boundary conditions.

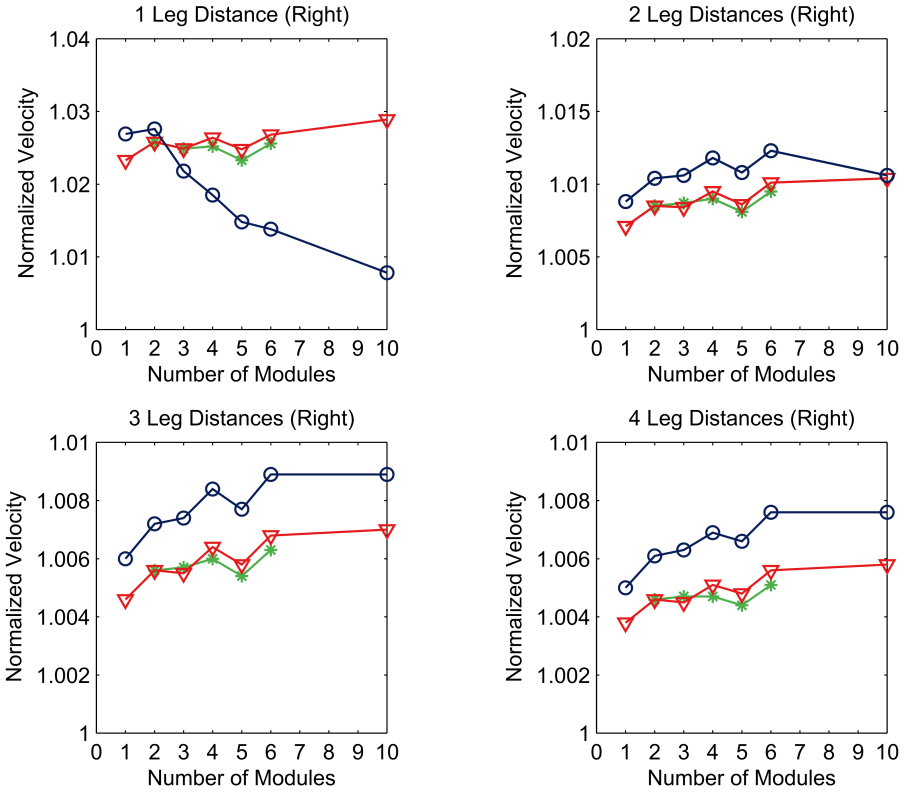

Figure 3.11: Side normalized velocity profile for different turbulence boundary conditions.

To investigate further, in Fig. 3.12 the entire velocity profile upstream of the mast is compared between the models with six modules included and two modules included. The results show that indeed, the effects of the turbulence boundary conditions are more intense closer to the mast, in the region with significant flow distortion. Being the area of interest in the current work, this makes their choice important. Another observation is that the increased number of modules has a marginal effect on the velocity profiles and is not as significant as the drag coefficient results. This can be attributed to the fact that the most significant difference is encountered in the close vicinity of the mast, where the drag coefficient is calculated.

All results of this study show that the difference of values between both methods of setting boundary conditions is almost constant given that the number of modules is more than one and the leg distance is two or higher (which is the region of interest as velocity deficit values required are 1% or 0.5%).

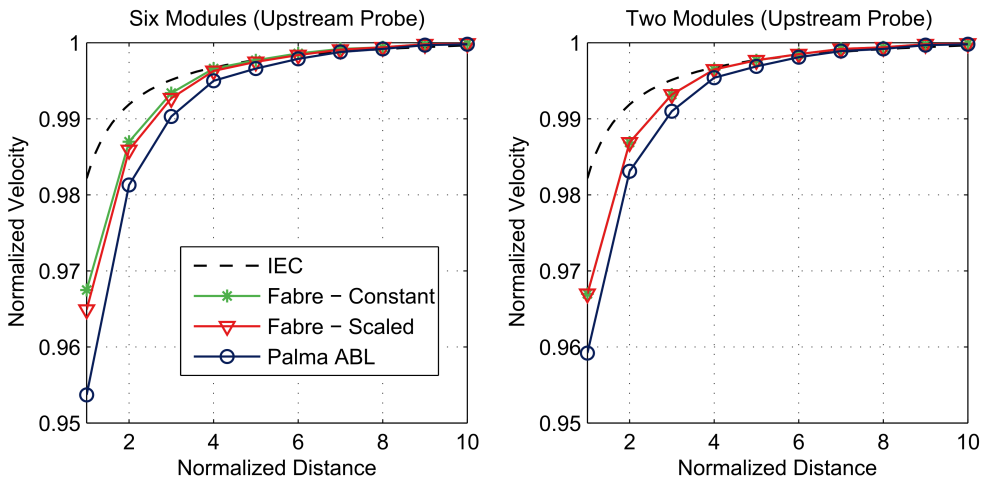

Figure 3.12: Upstream normalized velocity profile for different turbulence boundary conditions (comparison between 2 and 6 modules in representative section).

The velocity deficit profiles downstream of the mast are shown in 3.14. In the wake region, the turbulence boundary conditions are seen to not to have a significant effect compared to regions upstream and on the sides. This is expected, as the turbulence generated by the mast in its wake overpowers the freestream turbulence effects.

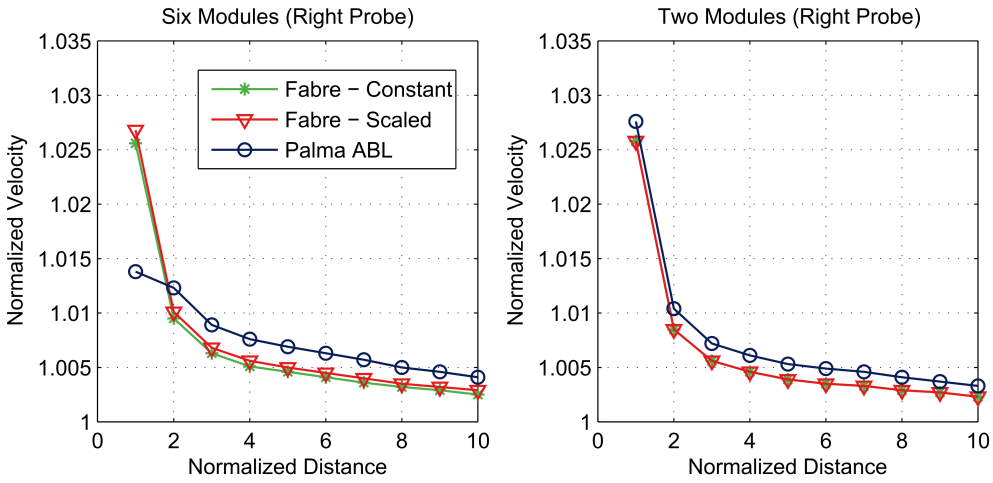

Figure 3.13: Side normalized velocity profile for different turbulence boundary conditions (comparison between 2 and 6 modules in representative section).

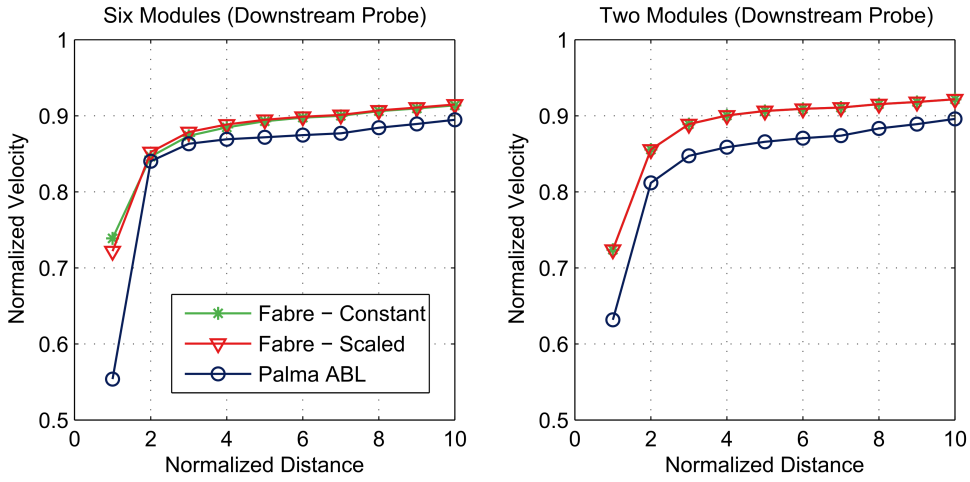

Figure 3.14: Downstream normalized velocity profile for different turbulence boundary conditions (comparison between 2 and 6 modules in representative section).

Up to this point it was shown that using freestream turbulence parameters from ABL profile theories resulted in a more intense flow distortion. The velocity deficit values upstream of the mast and speed-up values on the sides are seen to significantly vary when using ABL profiles and the approach of (Fabre et al., 2014). It was shown that the latter resulted in an underestimation of turbulence values, which is the reason corresponding results are closer to (IEC, 2005) which did not consider turbulence effects.

Fig. 3.15 and 3.16 show contour plots of normalized kinetic energy. The figures show that underestimated values of turbulence in the freestream by (Fabre et al., 2014) also results in reduced turbulence generated by the mast geometry. The same can be seen for normalized length scale contours in Fig. 3.17 and 3.18.

Given the previous findings, it is clear that freestream turbulence does has an effect on the flow distortion induced by the met mast. Higher turbulence in the freestream causes a more intense flow distortion. This is the reason why studies such as (Tusch et al., 2011) have suggested that (IEC, 2005) underestimates flow distortion effects. For purposes of suggesting guidelines of anemometer mounting, one should consider the worst-case scenario. Therefore, boundary conditions for subsequent CFD simulations were set according to ABL profiles given by (Palma et al., 2008). One final remark to make is that the use of the k-ϵ model in this study was speculated to overestimate the flow distortion effects. This was confirmed in the next section.

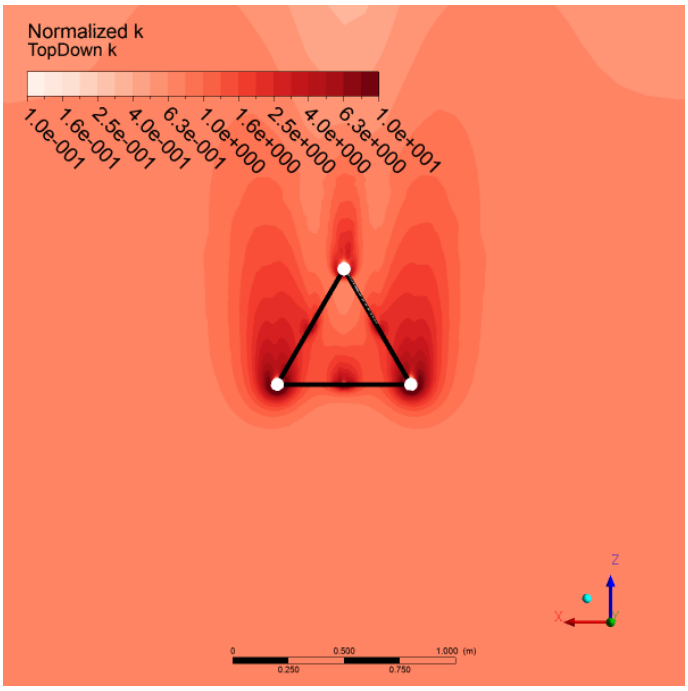

Figure 3.15: Normalized turbulence kinetic energy contour corresponding to freestream turbulence set according to ABL profile theories (Palma et al., 2008).

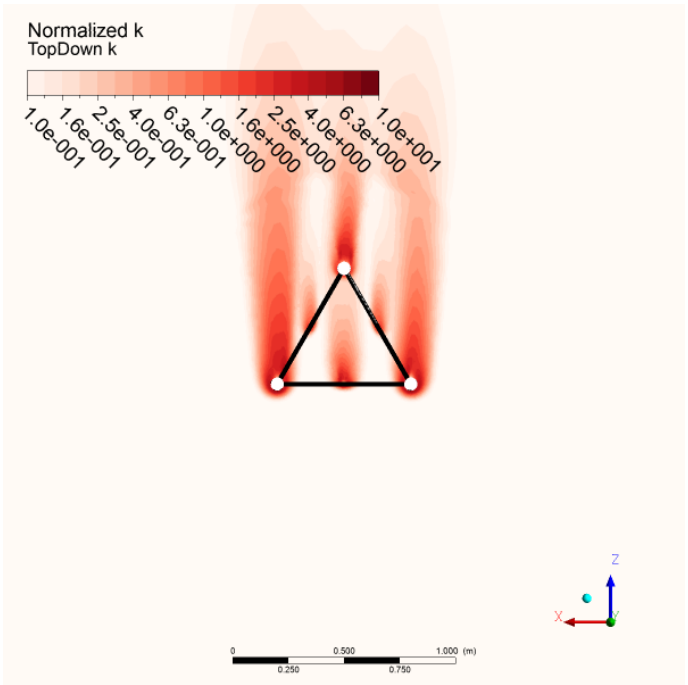

Figure 3.16: Normalized turbulence kinetic energy contour corresponding to freestream turbulence set according to approach of (Fabre et al., 2014).

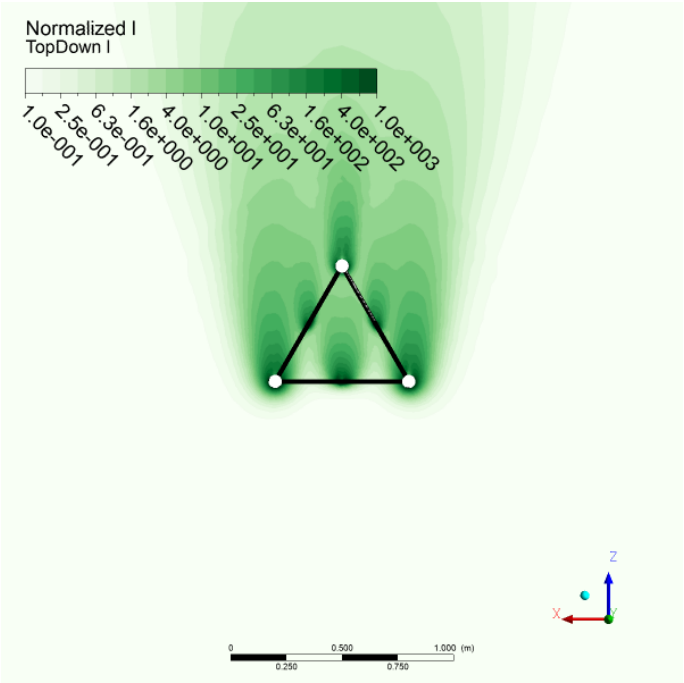

Figure 3.17: Normalized turbulence dissipation rate contour corresponding to freestream turbulence set according to ABL profile theories (Palma et al., 2008).

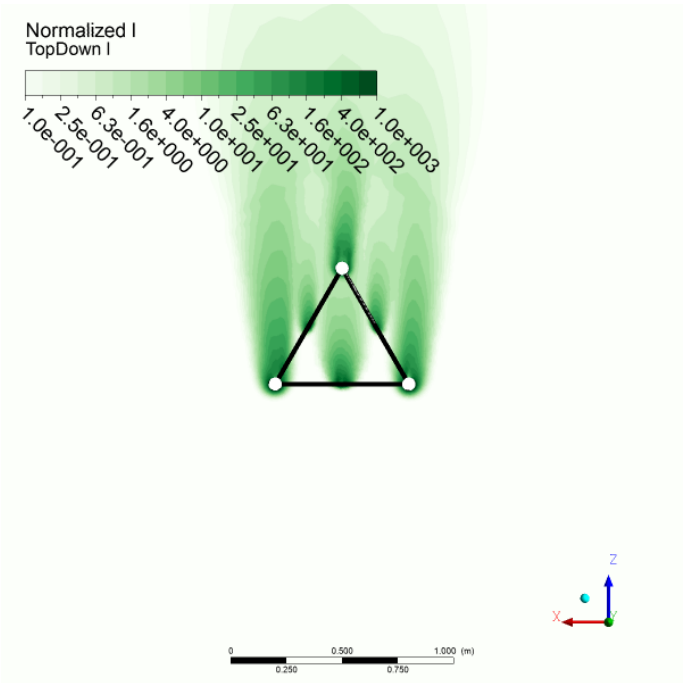

Figure 3.18: Normalized turbulence dissipation rate contour corresponding to freestream turbulence set according to approach of (Fabre et al., 2014).

3.3 Wind-Tunnel Simulation Studies

To determine the appropriate turbulence model, the wind tunnel experiments were modeled and simulated using CFD. This was done to eliminate any uncertainty caused by the difference in solidity ratios caused by the modification of geometry of the scaled down model due to manufacturing limitations as explained earlier. Fig. 3.19 shows a comparison between results obtained using the $k-\epsilon$ and $k-\omega$ turbulence models. The results show an excellent agreement between the wind tunnel measurements and the $k-\omega$ SST model, and prove the previously mentioned speculation of the $k-\epsilon$ model overestimating the interference effects. The variation in results at the lowest speed (1 ms^{-1}) can be attributed to low-Reynolds corrections needed in the turbulence models to simulate that range in wind speed. The choice of $k-\omega$ SST model is in agreement with all previously published studies (refer to 1.3.2).

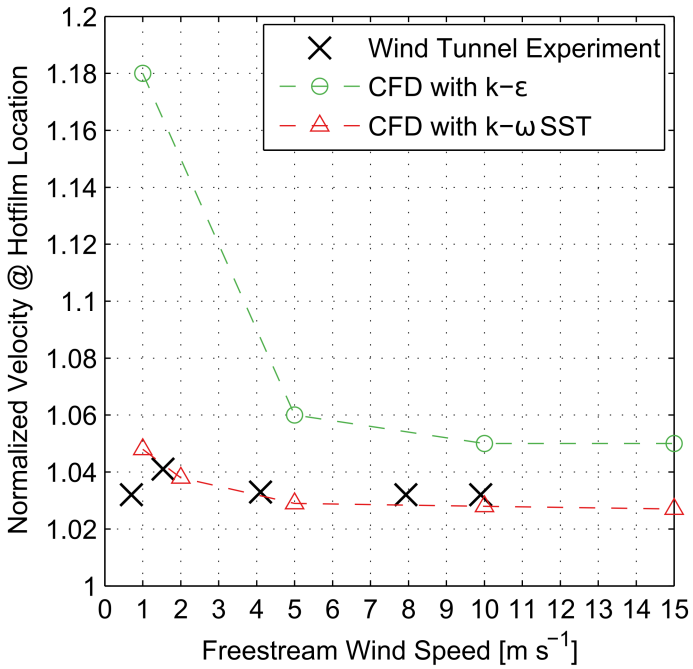

Figure 3.19: Comparison of CFD simulation using $k-\epsilon$ and $k-\omega$ SST turbulence models with wind tunnel experiments for different wind speeds.

Therefore, the $k-\omega$ SST model was used for all subsequent simulations.

3.4 Variation Along Atmospheric Boundary Layer

It was established that freestream turbulence has a significant effect on the flow distortion. Knowing that, an investigation was performed by taking values along the ABL profile provided by (Palma et al., 2008) with 15 meter intervals for a mast of 120 m height. This piecewise approximation is in accordance with the suggestion of (CEN, 2005) to calculate force values on a lattice structure. This study aims to check if the variation of turbulence parameters within the assumed (ideal) ABL would result in any significant variation of the flow distortion along the height of the mast.

The results for upstream and side velocity profiles are shown as a variation along mast height in Fig. 3.21 and Fig. 3.22, respectively. It is seen that at 1 leg distance from the mast center, there exists a variation in the deficit values along the mast height. This variation is within 0.5% between the lowest and highest locations on the mast. However, at leg distances of two and higher the variation is almost negligible. Since this is the region of interest (measurement error of $< 1\%$), the variation along the boundary layer height can be assumed to be negligible for anemometer placement purposes i.e., anemometer placement guidelines are not dependent on mounting height.

The final step is to again verify whether the significant different in values obtained for the $k-\epsilon$ was due to an overestimation caused by the model itself. The results upstream and on the side of the mast are compared for the highest and lowest location with the $k-\omega$ SST model, along with the solution from the $k-\epsilon$ model (at a center location, $y = 55$ m). The results in Fig. 3.23 and Fig. 3.24 indeed verify the speculation.

Since the variation along the mast height is marginal, one can therefore consider the center location (y= 55 m) given an ABL profile. This is the height considered in the subsequent analyses

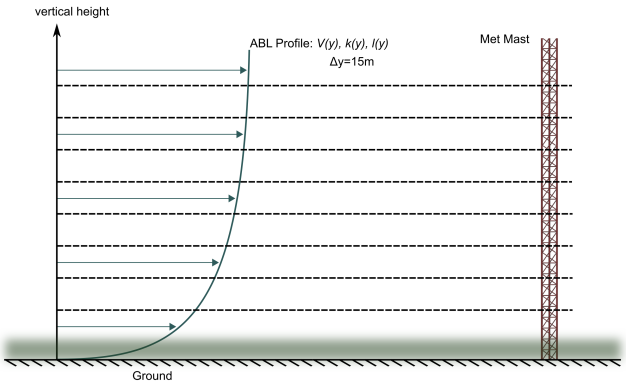

Figure 3.20: Piecewise discretization of ABL profile for use as boundary conditions.

of incident wind angle and different mast geometries.

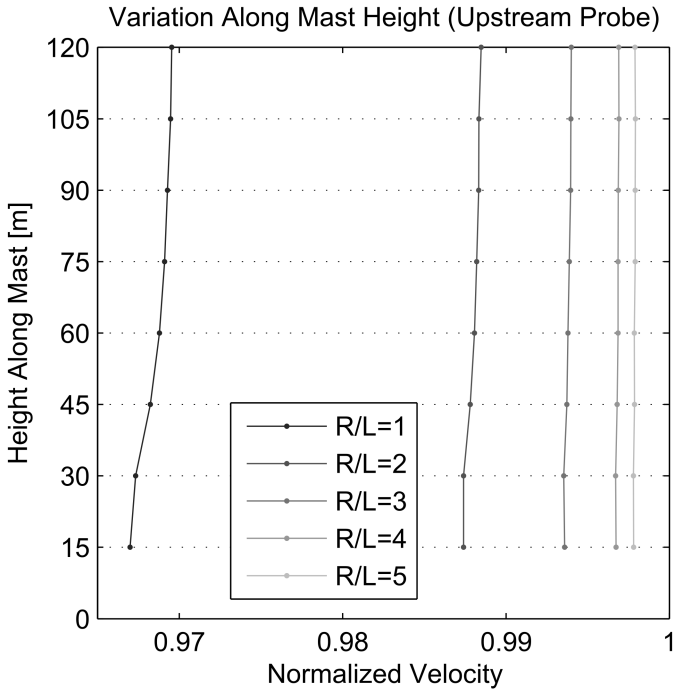

Figure 3.21: Variation of upstream velocity profile along mast height considering atmospheric boundary layer effects.

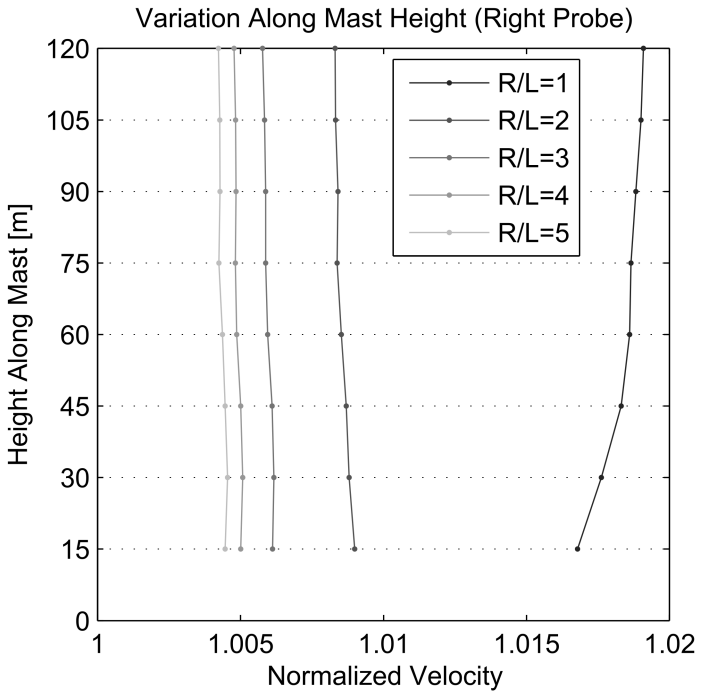

Figure 3.22: Variation of side velocity profile along mast height considering atmospheric boundary layer effects.

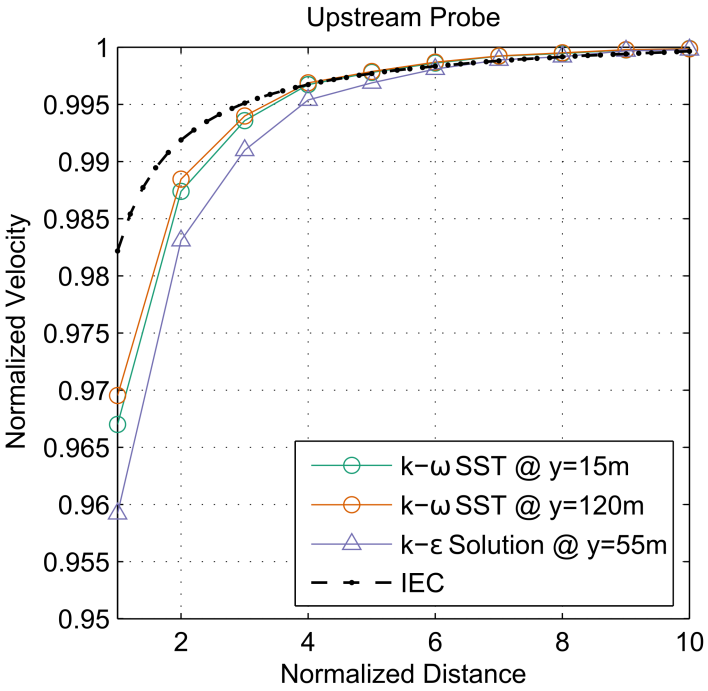

Figure 3.23: Comparison of upstream velocity profiles for $k-\epsilon$ and $k-\omega$ SST turbulence models considering atmospheric boundary layer effects.

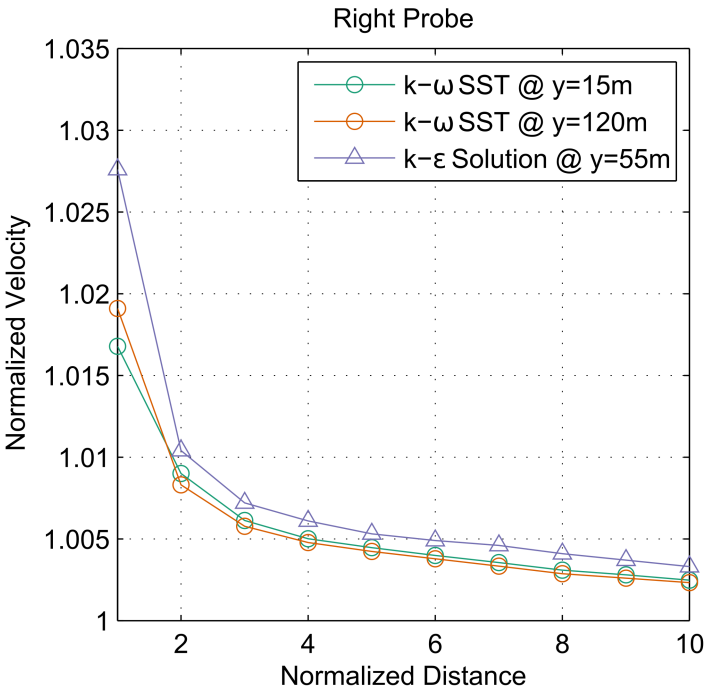

Figure 3.24: Comparison of side velocity profiles for $k-\epsilon$ and $k-\omega$ SST turbulence models considering atmospheric boundary layer effects.

3.5 Variation of Wind Incident Angle

Having fully constructed the numerical model for the CFD simulations, the effect of varying wind incident angle can now be studied. The test case is chosen as previously for an elevation of 55 meters. Values given by (Palma et al., 2008) ABL profile evaluated at that height are used as freestream conditions. The simulations are performed for both a triangular and a square mast (same leg distance). The results are taken upstream and on the side of the mast (fixed with varying wind direction, as is the case of mounting booms). The results compiled in Fig. 3.25, 3.26, 3.27, and 3.28; and show that the statement made by (IEC, 2005) about the default configuration ($\theta = 0°$) corresponding to the least flow distortion is not accurate.

Indeed, given a 90° measurement sector it is true that the least flow distortion is found at the default configuration, however by considering the full sector corresponding to the cyclic symmetry of the geometry, one finds that the least flow distortion is in fact at an angles where least solidity ratio is found. This proves all the speculations made at the beginning of the work. The same conclusion is made regardless of whether upstream or side velocity profiles are used.

By comparing Fig. 3.25 with Fig. 2.8 one can deduce that least flow distortion corresponds to incident wind angles with greatest solidity ratios. An inverse relationship could thus be constructed between flow distortion and projected area (dependent on incident wind angle). This is due to the fact that angles corresponding to lower values of solidity ratio are when one of the mast legs is located directly in the wake of another. This causes higher turbulence generation, and thus greater values of distortion.

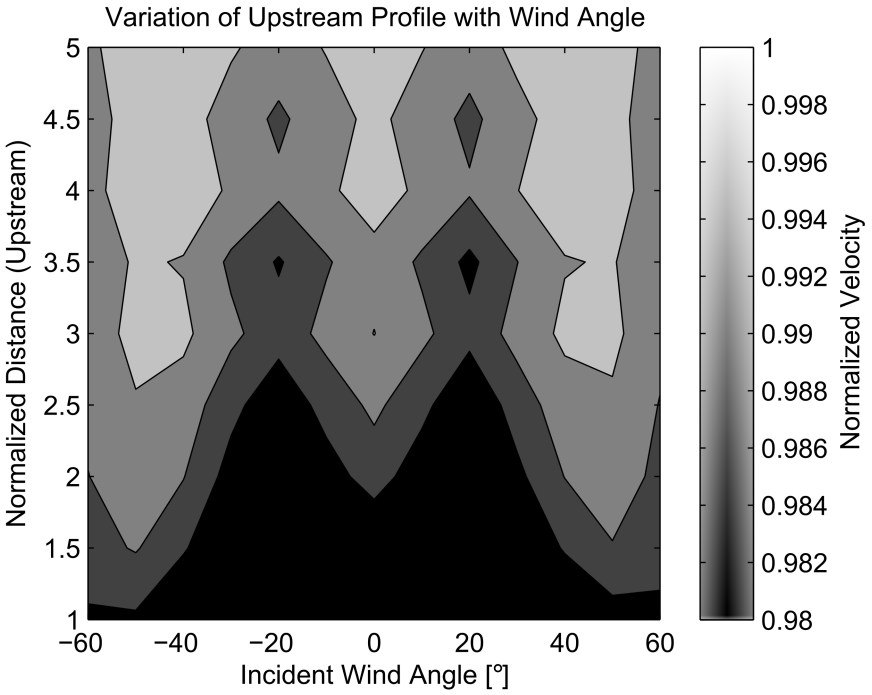

Figure 3.25: Triangular mast upstream velocity values for varying incident wind angles.

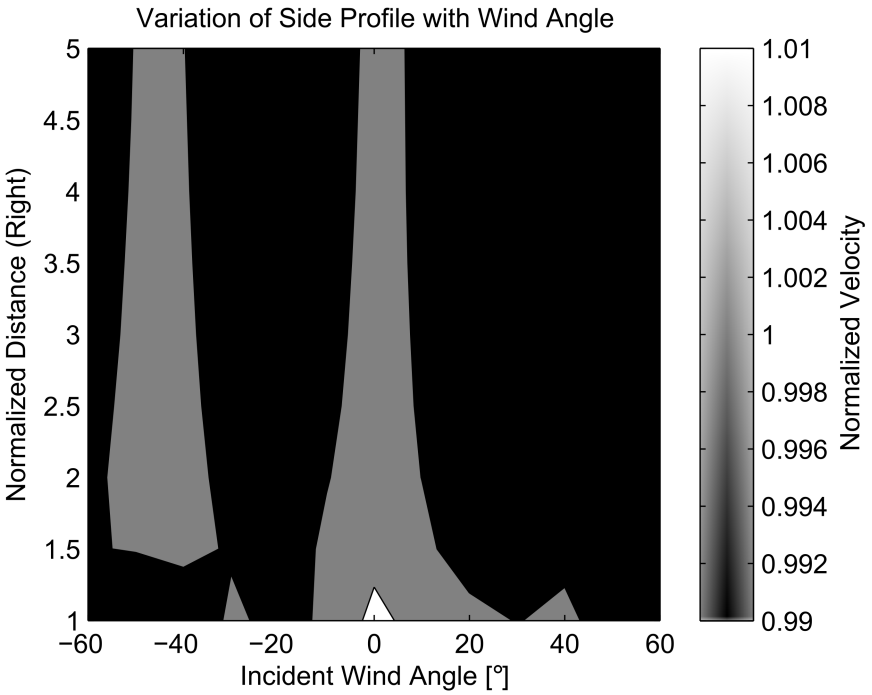

Figure 3.26: Triangular mast side velocity values for varying incident wind angles.

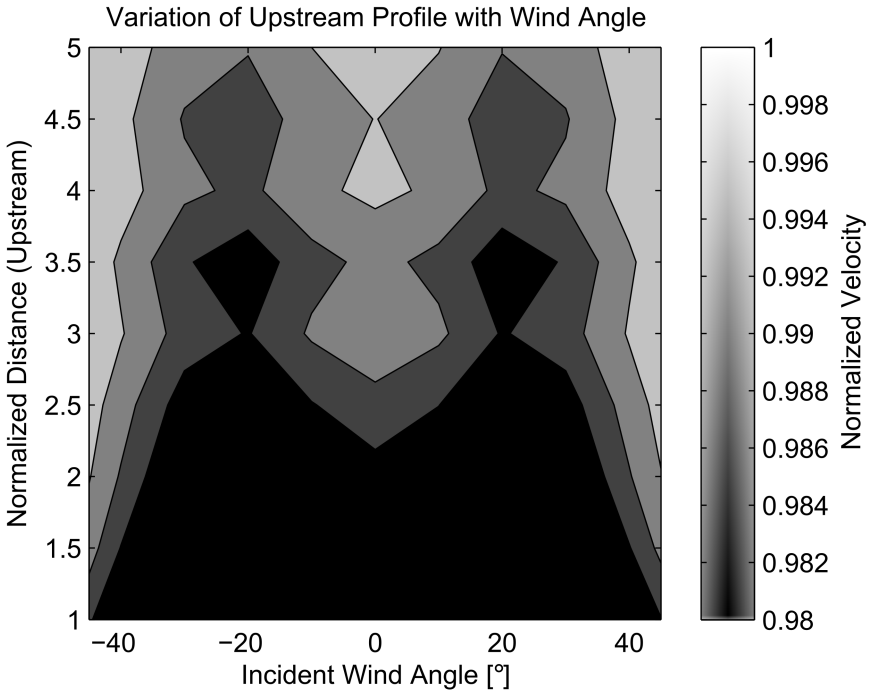

Figure 3.27: Square mast upstream velocity values for varying incident wind angles.

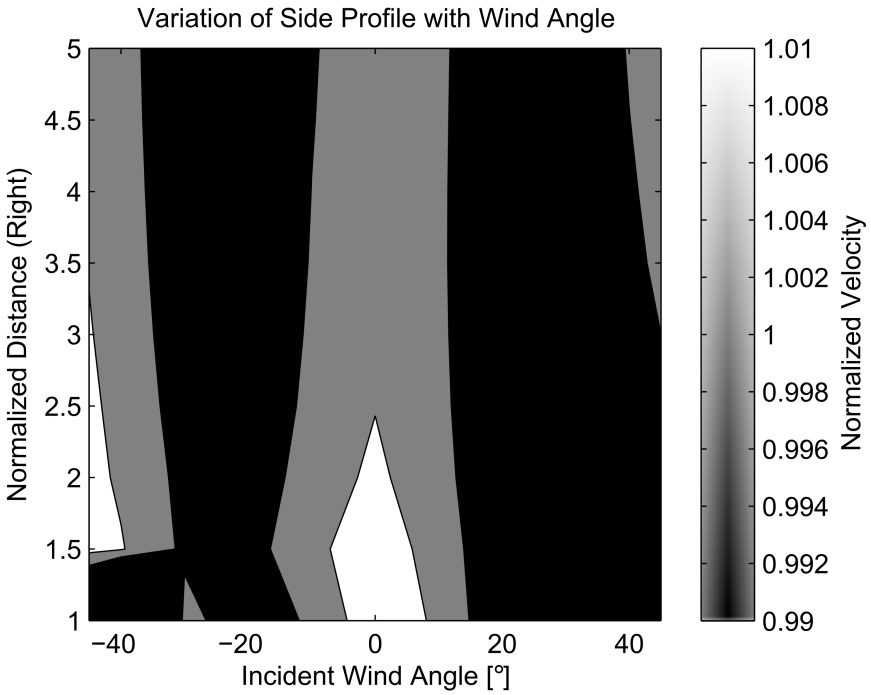

Figure 3.28: Square mast side velocity values for varying incident wind angles.

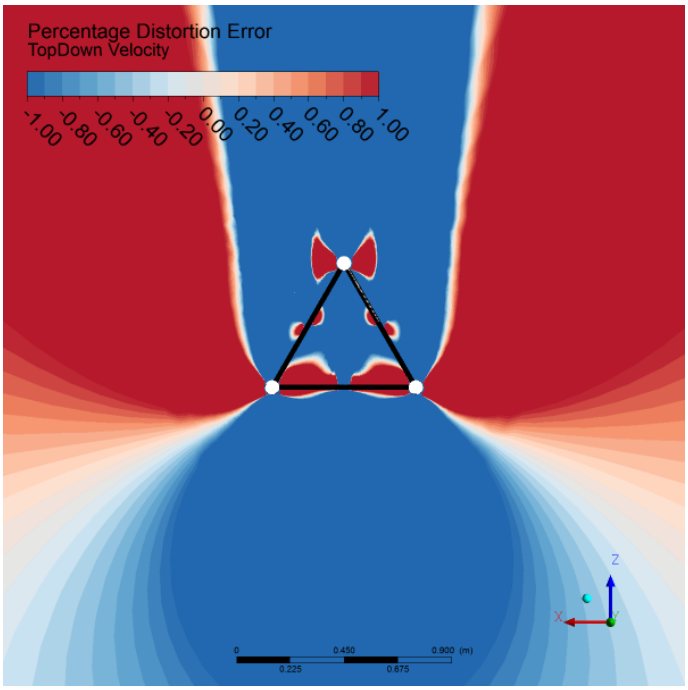

Figure 3.29: Measurement error contour plot for triangular mast with incident wind angle of 0°.

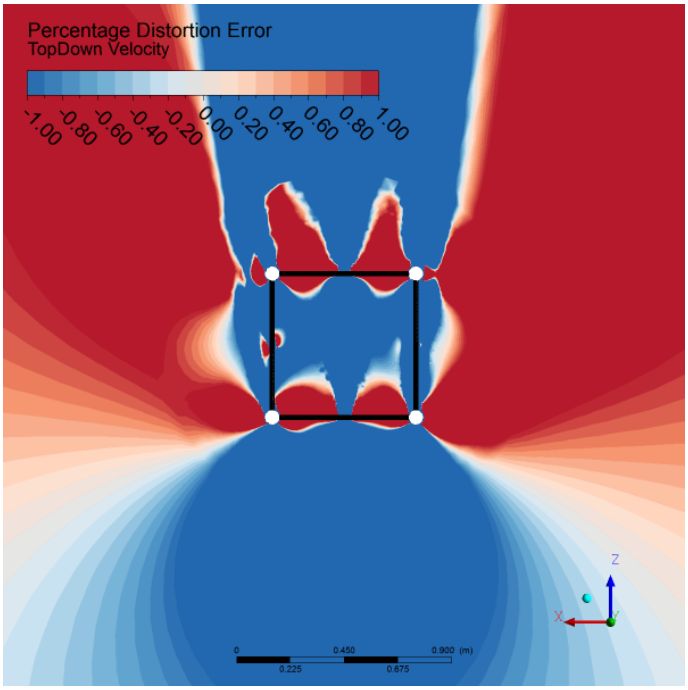

Figure 3.30: Measurement error contour plot for square mast with incident wind angle of 0°.

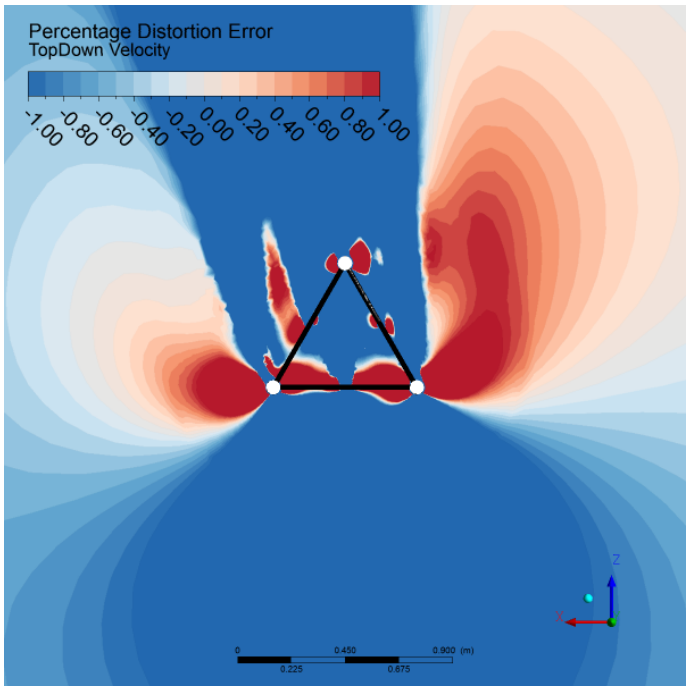

Figure 3.31: Measurement error contour plot for triangular mast with incident wind angle of 10°.

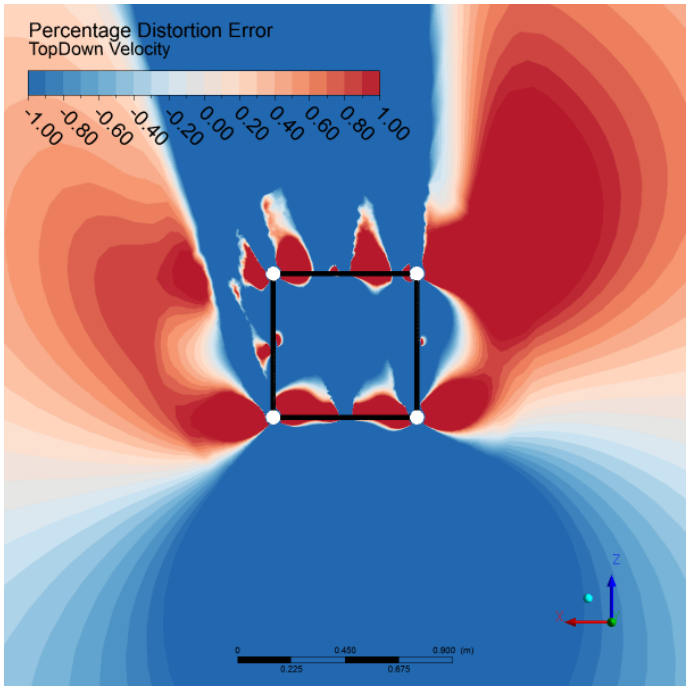

Figure 3.32: Measurement error contour plot for square mast with incident wind angle of 10°.

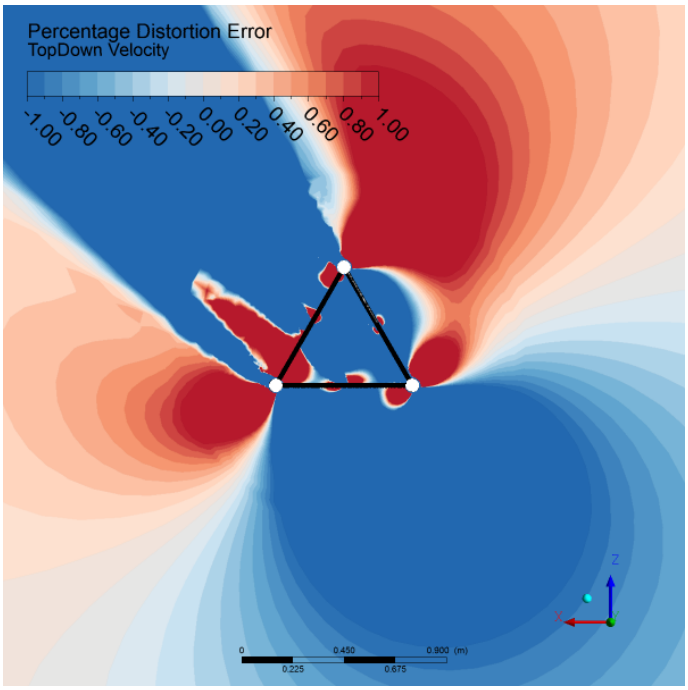

Figure 3.33: Measurement error contour plot for triangular mast with incident wind angle of 40°.

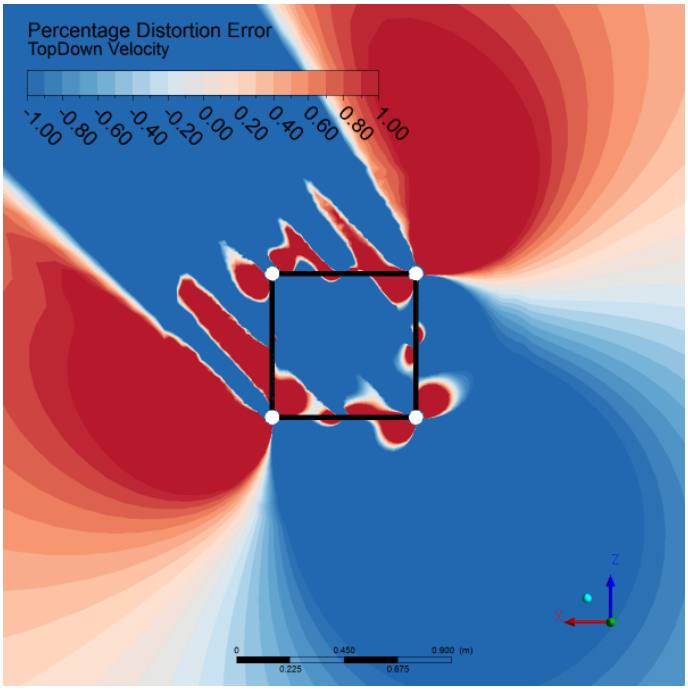

Figure 3.34: Measurement error contour plot for square mast with incident wind angle of 40°.

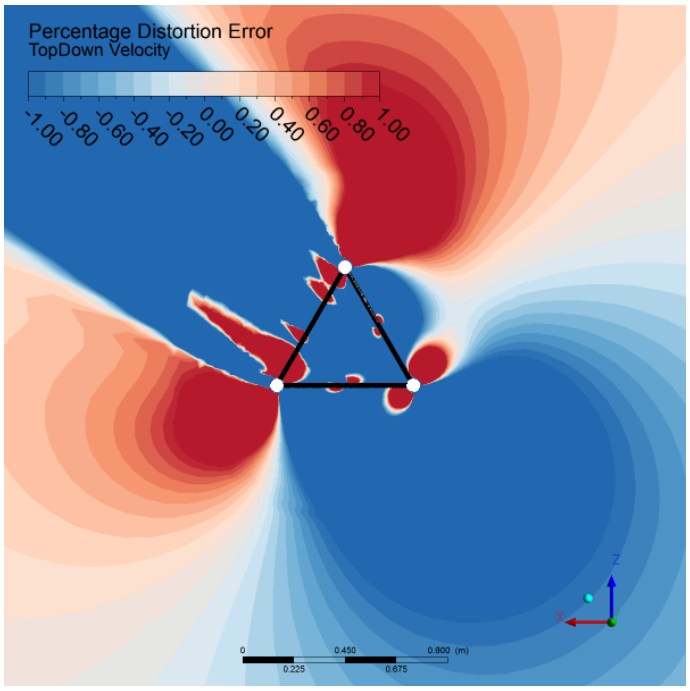

Figure 3.35: Measurement error contour plot for triangular mast with incident wind angle of 50°.

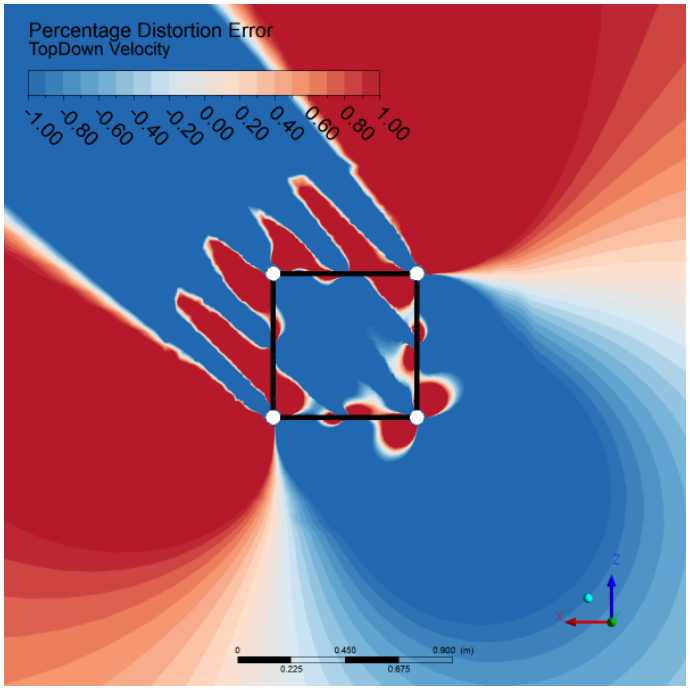

Figure 3.36: Measurement error contour plot for square mast with incident wind angle of 45°.

Chapter 4

Discussion

4.1 Conclusions

In Section 1.3.1, the shortcomings and limitations present in Annex G of IEC standard were listed and defined as the research focus of this study. After presenting all the results, several conclusions can be made in reference to the initial objectives. The conclusions drawn can be categorized in two groups. The first are in response to or criticism of previous literature, pointing out some incoherency in methods used, namely in CFD modeling. Those are listed below.

1. Previous studies have chosen an arbitrary number of modules in the mast representative section, whether for CFD simulations or wind tunnel experiments. The results of this study have shown that a minimum number of modules need to be included to adequately model the entire mast and eliminate boundary effects. This number can be determined by performing a preliminary CFD periodicity test. Note that the minimum number of segments required can be different for wind tunnel experiment and CFD simulation purposes. More details on this matter are found in Section 3.1.

2. The freestream turbulence parameters set at the CFD model boundaries were found to have a significant effect on the resulting flow field. Previous studies have modeled the problem as an arbitrary external flow problem, setting the boundary conditions as such in an arbitrary manner and thereby vastly underestimating freestream turbulence. This study has shown the problem should rather be considered as an atmospheric flow problem, and thus setting realistic freestream conditions corresponding to ABL profiles at the boundaries. More details on this matter are found in Section 3.2.

3. Wind tunnel experiments have shown that the distortion might be a slight dependency on velocity low Reynolds number. Previous studies and the IEC standard have stated that no such dependency exists. This was not further investigated by this work and thus needs further verification. More details on this matter are found in Section 3.3.

4. The $k-\omega$ SST turbulence model was found to be the most adequate two-equation RANS model for this problem. This is in accordance with all previous studies. More details on this matter are found in Section 3.3.

The second group of conclusions are direct implications this work has on anemometer placements guidelines.

1. The variation of the shadow zone along the mast height due to the ABL profile was found to be marginal and can be neglected for heights above 15 meters. However, note that an idealized boundary layer was assumed in this work, ignoring effects such as stratification. However, the effects of freestream turbulence need to be considered as they were found to significantly affect the flow distortion caused by met masts. More details on this matter are found in Section 3.4.

2. Flow distortion effects were found to be dependent on incident wind angle. The IEC standard mentions that the standard configuration correspond to least flow distortion. The results show that this might not be true, as an inverse relation between solidity ratio (as a function of angle) and wind angle was found i.e., angles corresponding to lowest solidity ratios were found to exhibit highest flow distortion values. This is due to the fact that low solidity ratios are caused by a lineup of two of the structure legs, reinforcing turbulence generation and thereby intensifying induced flow distortion.

3. A direct correlation between velocity deficit values upstream and those of the sides was found. The distortion effects upstream are of greater magnitude. This implies that the usage of upstream values as a guidelines for anemometer mounting as in the case of IEC is convenient, and further provides a safety factor. More details on this matter are found in Section 3.5.

4.2 Recommendations

To summarize, this work has filled a research gap that was present in the CFD modeling strategies available for the current problem. It was shown that this problem should be modeled as an atmospheric flow problem by considering appropriate freestream turbulence conditions, which were found to have a significant effect on the distortion effects.

The IEC standard provided an expression for velocity deficit values in terms of the solidity ratio of the mast at standard configuration (θ=0°). It was shown that there exists a dependency on the solidity also as a function of wind incident angle i.e., $t(\theta)$ with minimum flow distortion inversely proportional thereof. Follow-up studies on this study should conduct a parametric study on this effect, attempting to incorporate wind angle into the velocity deficit expression. This could be done more conveniently by using the CFD modeling recommendation provided by this work, and thus future work could directly investigate the phenomenon.

appendices are not used

References

Eurocode 1: Actions on structures - part 1-4: General actions - wind actions. CEN EN 1991-1-4, European Committee for Standardization, 2005.

Wind turbines – part 12-1: Power performance measurements of electricity producing wind turbines. IEC 61400-12-1, International Electrotechnical Commission, Geneva, Switzerland, December 2005.

Eurocode 3: Design of steel structures - part 3-1: Towers, masts and chimneys – towers and masts. CEN EN 1993-3-1, European Committee for Standardization, 2006.

ANSYSInc. *ANSYS Fluent Theory Guide*. ANSYS, Inc., 2011.

W.D. Bachalo and D. A. Johnson. Aiaa journal. *Journal of Wind Engineering and Industrial Aerodynamics*, 24(3):437–443, 1986.

Janet F. Barlow, James Harrison, Alan G. Robins, and Curtis R. Wood. A wind-tunnel study of flow distortion at a meteorological sensor on top of the bt tower, london, uk. *Journal of Wind Engineering and Industrial Aerodynamics*, 99(9):899–907, 2011.

J. H. Bell and R. D. Mehta. Boundary-layer predictions for small low-speed contractions. *American Institute of Aeronautics and Astronautics Journal*, 27:372–374, 1989.

Marshall Bern and Paul Plassmann. Mesh generation. In *Handbook of Computational Geometry*. Elsevier Science, 2000.

Alfred K. Blackadar. The vertical distribution of wind and turbulent exchange in a neutral atmosphere. *Journal of Geophysical Research*, 67(8):3095–3102, 1962.

Karl J. Eidsvik. Prediction errors associated with sparse grid estimates of flows over hills. *Boundary-Layer Meteorology*, 127:153–172, 2008.

S. Fabre, M. Stickland, T. Scanlon, A. Oldroyd, D. Kindler, and F. Quail. Measurement and simulation of the flow field around the fino 3 triangular lattice meteorological mast. *Journal of Wind Engineering and Industrial Aerodynamics*, 130:99–107, 2014.

Robert N. Farrugia and Tonio Sant. Modelling wind speeds for cup anemometers mounted on opposite sides of a lattice tower: A case study. *Journal of Wind Engineering and Industrial Aerodynamics*, 115:173–183, 2013.

Finn E. Jørgensen. *How to measure turbulence with hot-wire anemometers*. Dantex Dynamics, 2002.

Emrah Kulunk. Aerodynamics of wind turbines. *Fundamental and Advanced Topics in Wind Power*, 2011.

William David Lubitz. Effects of tower shadowing on anemometer data. *Proceedings of 11th Americas Conference on Wind Engineering*, 2009.

R. D. Mehta and P. Bradshaw. Design rules for small low speed wind tunnels. *The Aeronautical Journal of the Royal Aeronautical Society*, 73:443–449, 1979.

J. M. L. M. Palma, F. A. Castro, L. F. Ribeiro, A. H. Rodrigues, and A. P. Pinto. Linear and nonlinear models in wind resource assessment and wind turbine micro-siting in complex terrain. *Journal of Wind Engineering and Industrial Aerodynamics*, 96(12):2308–2326, 2008.

Auhas V. Patankar. *Numerical Heat Transfer and Fluid Flow*. Hemisphere Publication Corporation, 1980.

Pratish P. Patil and Shaligram Tiwari. Effect of blockage ratio on wake transition for flow past square cylinder. *Fluid Dynamics Research*, 40(40):753–778, 2008.

Dimitri Perrin, Niall McMahon, Martin Crane, Heather J. Ruskin, Lawrence Crane, and Brian Hurley. The effect of a meteorological tower on its top-mounted anemometer. *Applied Energy*, 84:413–424, 2007.

Milada L. Pezo and Vukman V. Bakić. Numerical determination of drag coefficient for guyed mast exposed to wind action. *Engineering Structures*, 62-63:98–104, 2014.

S. B. Pope Pope. *Turbulent Flows*. Cambridge University Press, 2000.

P.J. Richards and R.P. Hoxey. Appropriate boundary conditions for computational wind engineering models using the k-ϵ turbulence model. *Journal of Wind Engineering and Industrial Aerodynamics*, 46-47:145–153, 1993.

H. Schlichting. *Boundary-Layer Theory*. McGraw-Hill Book Company, 1968.

M Tusch, C Masson, and P Héraud. Modeling of turbulent atmospheric flow around tubular and lattice meteorological masts. *Journal of Solar Energy Engineering*, 133(1), 2011.